Towards an Optoelectronic Characterization of Molecules by Nanoscale Gold Antennas

Inauguraldissertation

zur
Erlangung der Würde eines Doktors der Philosophie
vorgelegt der
Philosophisch-Naturwissenschaftlichen Fakultät
der Universität Basel

von

Martin **Toni Fröhlich**
aus Berlin (Deutschland)

Basel, 2014

Genehmigt von der Philosophisch-Naturwissenschaftlichen Fakultät
auf Antrag von
PD Dr. Michel Calame
Prof. Dr. Christian Schönenberger
Prof. Dr. Olivier Martin

Basel, den 17. September 2013

Prof. Dr. Jörg Schibler
Dekan

Contents

Chapter 1

Introduction – Plasmonics and Molecular Electronics

In 1974 Aviram and Ratner proposed theoretically a molecule which contains both an acceptor and donor part separated by a spacer group [1]. This molecule can act as a rectifier or diode when an electric current is passing through. In the past 20 years new techniques in nanoscience made it possible to study the electric current through small objects. As a result, the field of molecular electronics has been explored more and more experimentally [2, 3].

Ideally a single conductive molecule is bridging a gap between two electrode tips which are in most cases made of gold. Experimental techniques allowing this are the scanning tunneling microscope (STM) already realized in 1981 by G. Binning and H. Rohrer [4, 5] and the break junction technique by mechanical force, chemical etching or electromigration on a sub-micrometer gold constriction [6].

The molecule as the central unit can be a rectifier, a transistor or a switch changing its electrical properties by interaction e.g. with light, magnetic field, temperature or electrical potential. Therefore molecular electronics is a fascinating new field in nanoscience which could lead to concrete future applications.

Optically active molecules are a very interesting object in molecular electronics. They can switch by incident light between two states which conduct the electrical current differently [7, 8]. Here, the light is an additional physical parameter which substantially enriches the field of molecular electronics.

One way to realize an optoelectronic device is by using the plasmonic behaviour of small metal particles. Metal nanoparticles and especially made of gold can interact with light by inducing a localized surface plasmon inside the metal [9–11]. This creates an electric near-field around the nanoparticles which is much higher than the incident field. We will name the localized surface plasmon for simplicity “a plasmon” in the following chapters.

The plasmonic behaviour of nanoparticles can be used in various kinds of applications. The plasmon energy or surface plasmon resonance (SPR) is changed by molecules attaching the gold surface so that these molecules are optically detected [12]. Other applications are light phase manipulations [13], extreme light concentration for nonlinear processes [14] or a new design of solar cells which leads to a higher efficiency [15].

The high electric near-field can excite a molecule close to the metal nanoparticle, e.g. in surface enhanced Raman scattering (SERS) [16, 17]. SERS measurements were also demonstrated on electromigrated junctions [18]. As the next step it was possible to use these junctions for in situ electrical measurements of molecules [19, 20]. A gold break junction with sub-nanometer gaps for plasmonic applications could be achieved with an atomic force microscope (AFM) experiment [21]. This could lead to a mechanically controllable break junction for investigation of optically active molecules interacting with plasmonic gold electrodes.

In this thesis we discuss the electrical properties of molecules which can be optically excited and anchored to gold electrodes by chemical groups on both ends. Hence, the molecule can bridge a small gap in which the optical near-field enhancement plays an important role. Gold dipole antennas can create a highly enhanced local electric field inside such a narrow gap and therefore act as a platform to excite optically a bridging molecule. We study these nanoscale antennas by their gold photoluminescence spectra in order to learn more about the plasmonic behaviour.

The thesis is structured as following:

- In **Chapter 2** we focus on electrical measurements of benzodifuran based molecules.
- **Chapter 3** introduces the optical setup and describes basic aspects of the photoluminescence measurements.
- In **Chapter 4** we discuss the gold photoluminescence of single monopole antennas as a function of size and shape.
- **Chapter 5** presents the gold photoluminescence of dipole antennas with the main focus on interparticle interaction.

Chapter 2

Conductance Measurements of Benzodifuran Derivatives

Optically active molecules within molecular electronics are interesting objects to study. Here, benzodifuran derivatives terminated by anchor groups are one examples. Interaction with light could alter the electric transport properties of these molecules [22] and therefore act as an additional switch. We investigated two of these optically active molecules in a mechanically controllable break junction (MCBJ) setup.

2.1 Benzodifuran Derivatives as Optically Active Molecules

We studied two benzodifuran molecules synthesized by the group of Silvio Decurtins (University of Berne). The backbone of these molecules are derived from oligo(phenylene ethynylene) (OPE) where on the central benzene ring are two furan rings attached (Fig. 2.1). The hexyl groups on both furan rings renders the solubility in several organic solvents and the cyanide groups extend the π-electron system over the molecule [23]. The molecule was either capped by pyridyl or acetylthiol groups on both ends and can therefore bridge a gap between two gold electrodes.

The central benzodifuran unit acts as an optical core. In Fig. 2.2 the UV-VIS absorption and emission spectrum of the pyridyl capped molecule (BDF_{NN}) are shown. Here, the maximum of absorption and emission is at $\lambda \approx 480$ nm and 530 nm, respectively. The HOMO-LUMO gap was determined with 2.44 eV. The energy gap for the acetylthiol capped molecule (BDF_{SS}) is with 2.53 eV slightly higher [23].

Benzodifuran derivatives can be used as building blocks [24, 25]. A polymerization alters the optical properties significantly and leads to a multitude of possibilities [26].

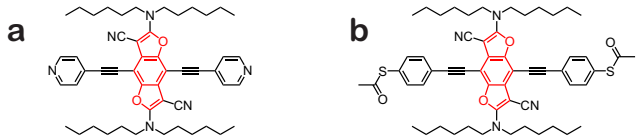

Figure 2.1: Two benzodifuran (BDF) derivatives which were measured in this work. The optically active core is red highlighted: **(a)** Pyridyl-terminated (BDF_{NN}) and **(b)** acetylthiol-terminated molecule (BDF_{SS}).

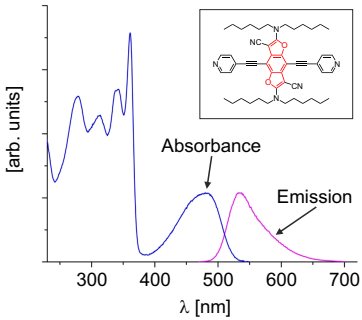

Figure 2.2: Absorbance and emission of the pyridyl-terminated derivative (BDF_{NN}). This optical characterization in dichloromethane was done by the group of Silvio Decurtins (University of Berne).

2.2 Mechanically Controllable Break Junction

When a gold wire is mechanically stretched in a narrow constriction, it eventually breaks and forms a nanometer-sized gap. We used a steel substrate with lithographically fabricated gold wires. These gold wires can break in a sub-micrometer constriction while the substrate is substantially bent.

Fabrication

Break junction samples were fabricated on a thin steel substrate by electron-beam lithography. In the metallization process titanium was angular deposited in order to receive a pure gold constriction which can finally be broken. Afterward a photodefinable polyimide layer was added which covers the electrical contacts beside a 10 µm wide channel (Fig. 2.3b,c). This reduces the leakage current during the measurements. Right before measuring the insulating polyimide was

dry etched in a O_2/CHF_3 plasma to create a free-standing gold bridge (Fig. 2.3c). More details can be found in the appendix A.

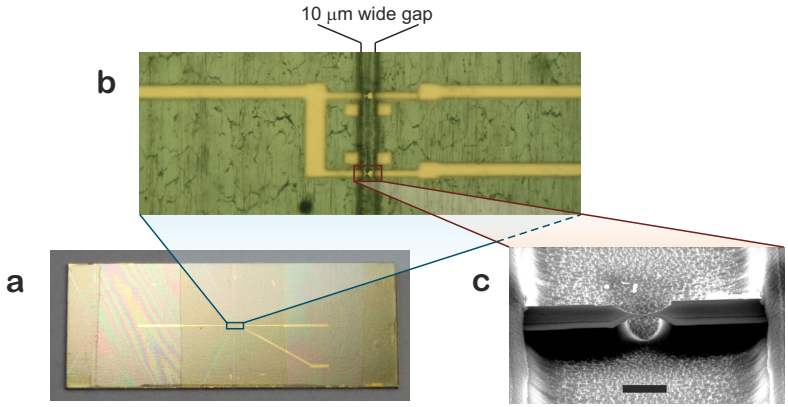

Figure 2.3: **(a)** Break junction sample with two independent junctions. **(b)** An optical zoom-in shows a 10 µm wide gap inside the polyimide insulation layer. **(c)** Further zoom-in illustrates the free-standing gold bridge of a typical sample. The scale bar is 2 µm. This SEM image was kindly provided by Jan Brunner [27].

Measurements and Setup

A photo and the electric circuit of the setup are shown in Fig. 2.4. The whole measuring unit is covered by a metallic chassis in order to reduce the electronic noise. The substrate is fixed on both ends and bent by a central push rod. At a certain bending curvature of the substrate the gold bridge breaks and forms a sub-nanometer gap d. Each further lifting of the push rod ($\triangle z$) and substrate bending result in an additional gap separation $\triangle d$. The attenuation factor $a_c = \triangle d / \triangle z$ was determined to be $1.5–4 \cdot 10^{-5}$ [28]. More details can be find elsewhere [29].

We first measured the conductance vs. position of the push rod z in pure solvent in order to test whether the junction is clean enough for molecular measurements. At the conductance $G = G_0$ we see a plateau which corresponds to a pull-out of a single-atom-width gold wire right before the gap formation. Here, the value $G_0 = 2e^2/h$ is the conductance quantum. During the measurements the gap is repeatedly opened and closed in a few hundreds of cycles. During the closing process the electrodes are compressed together at a conductance of $20\,G_0$. This ensures the formation of a clean gap in the next cycle.

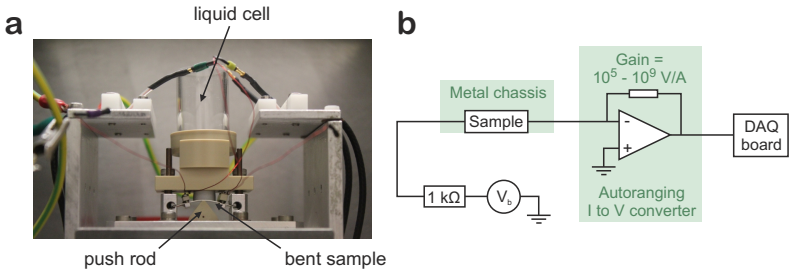

Figure 2.4: (a) Photograph of the MCBJ setup with the 3-point bending mechanism. The mounted liquid cell, a bent sample and the push rod are indicated. **(b)** Schematics of the electronic setup including a voltage source (V_b). The output voltage of the I to V converter is measured by a data acquisition (DAQ) board which is connected to a computer.

Analysis

We visualized the experiments with different kinds of diagrams. For each cycle we can plot a logarithmic histogram of conductance values and the conductance vs. push rod displacement z. These diagrams monitor the quality of the junction over time. Finally we summarized all consecutive conductance traces of a series in histograms. A 2D histogram is calculated by overlapping all traces pinned at $G_{ref} = 0.5\,G_0$ and a certain displacement z. More details are illustrated in the appendix D.

2.3 Experimental Results

We measured thiol- and pyridyl-terminated molecules (see table 2.1) in our MCBJ setup. The measurements were done in two different solvents, dichloromethane

in	**dichloromethane**	**THF/mesitylene 1:4 v/v**
BDF_{NN}	1 sample	2 samples
BDF_{SS}	1 sample	3 samples

Table 2.1: Table of all break junction experiments discussed in this work. We used an aromatic (mesitylene) as well as a non-aromatic (dichloromethane) solvent in the measurements.

and tetrahydrofuran (THF)/mesitylene (1:4 v/v). The molecular concentration (BDF) were 250 µM, except in the experiment with BDF_{NN} in dichloromethane (80 µM). The bias voltage U_{bias} was always fixed to 0.2 V. The push rod speed were 31.2 µm/s and 100 µm/s (only BDF_{NN} in THF/mesitylene) which corresponds to a gap opening of 0.5–1.3 nm/s and 1.5–4 nm/s, respectively [28].

2.3.1 Benzodifuran-dipyridiyl (BDF_{NN})

In the following discussion we focus on opening traces. The 2D histograms (Fig. 2.5) of traces in dichloromethane as well as in THF/mesitylene show no clear evidence of molecular conductance plateaus. The background level at approximately $10^{-6}\,G_0$ is dependent on the junction, the noise level of the environment and the solvent. Only for the measurements in dichloromethane (Fig. 2.5b) exist between $10^{-4}\,G_0$ and $10^{-3}\,G_0$ a higher concentration of counts. In order to investigate this interval in detail we first classified manually traces with and without possible molecular plateaus. 31 % of all traces contain a visible plateau (in dichloromethane), and also some of the traces in THF/mesitylene. In Fig. 2.6 are the 1D histogram of traces with (Fig. 2.6c) and without (Fig. 2.6a) plateaus presented. The conductance values in the interval $(10^{-4}...10^{-3})\,G_0$ are slightly more pronounced for traces containing plateaus but still no clear peak is observable.

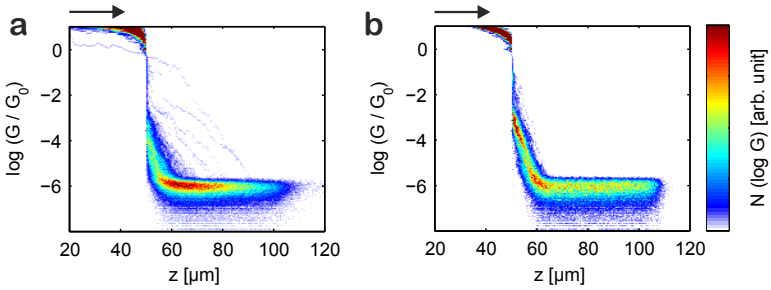

Figure 2.5: 2D histograms of **(a)** 400 and **(b)** 200 consecutive opening traces. The concentration of BDF_{NN} was **(a)** 250 µM in THF/mesitylene and **(b)** 80 µM in dichloromethane. The push rod speed was set to 31.2 µm/s. Both histograms do not have any clear plateau region. The measurement in dichloromethane shows a higher concentration of counts in the conductance interval between $10^{-4}\,G_0$ and $10^{-3}\,G_0$.

We can gain more information by calculating the average conductance $(\langle G\rangle/G_0)$ and length $(\triangle z)$ [µm] for each plateau, like it is illustrated in Fig. 2.6d. A plot of the

length vs. the average conductance in Fig. 2.7 makes the distribution of plateaus clearer. Two conductance intervals are marked in this diagram. About half (52 %) of all plateaus are present in the logarithmic interval ($\log_{10}(\langle G\rangle/G_0)$ = -4.1...-2.9) whereas only one third (32 %) are in the interval ($\log_{10}(\langle G\rangle/G_0)$ = -5.7...-4.7).

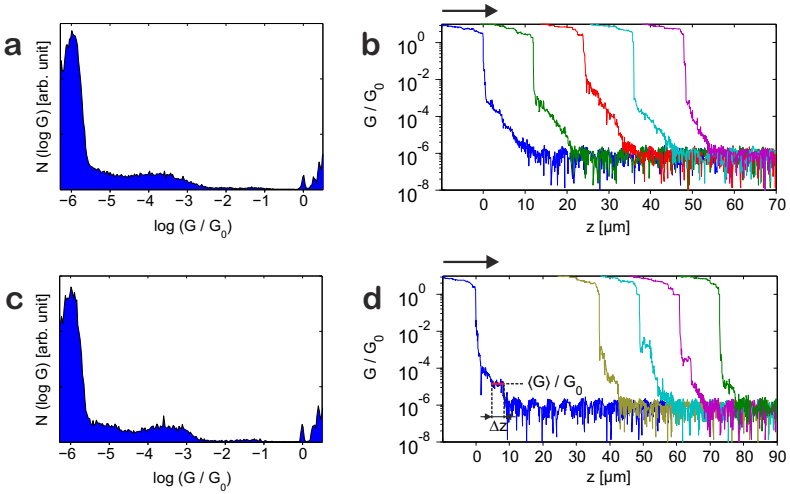

Figure 2.6: (a,c) 1D logarithmic histograms of conductance values. **(a,b)** All 139 opening traces have no visible plateau. **(c,d)** 61 opening traces contain conductance plateaus. **(b,d)** Typical measured opening traces as examples. The concentration of BDF_{NN} was 80 µM in dichloromethane and the push rod speed was set to 31.2 µm/s. The histogram **(c)** with plateaus shows a slightly pronounced peak in the interval ($10^{-4}...10^{-3}$) G_0. We studied the distribution of individual plateaus. For this purpose, we estimated the length ($\triangle z$) and calculated the average conductance ($\langle G\rangle/G_0$) like it is marked in **(d)**.

The traces contain no plateau longer than 5 µm which would correspond to an electrode separation of 0.075–0.2 nm [28]. These very short plateaus indicate that the molecule anchors very weakly on the gold electrodes. Even when we increased the push rod speed up to 100 µm/s we could not increase the plateau length. The pyridyl end groups in oligo(phenylene ethynylene) (OPE_{NN}) are known to bind strongly on gold. The conductance of OPE_{NN} was measured to be $1.2 \cdot 10^{-5}\ G_0$ (U_{bias} = 0.1 V) [27].

It is possible that the pyridyl-Au bonds are weakened by the furan rings compared to OPE_{NN}. Songmei Wu discussed the effect of side groups on the binding

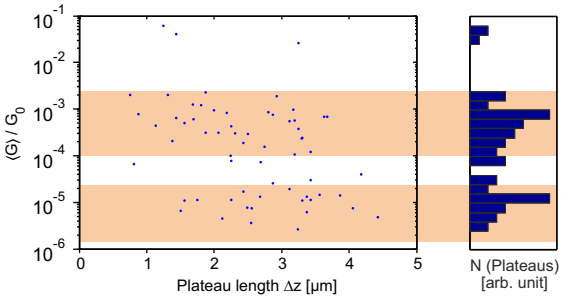

Figure 2.7: Plateau statistics of 61 opening traces and (right) histogram of conductance plateaus. The concentration of BDF_{NN} was 80 µM in dichloromethane. We see two main intervals where plateaus are located. In the lower interval ($\log_{10}(\langle G\rangle/G_0)$ = -5.7...-4.7) are 32 % and the upper interval ($\log_{10}(\langle G\rangle/G_0)$ = -4.1...-2.9) contains 52 % of all plateaus. We speculate that each interval corresponds to a different binding modification of the molecule on gold electrodes.

affinity of amine (NH_2) anchors [29]. She observed a higher affinity to gold and a higher molecular conductance. Pyridine is binding by donating the electron lone pair of nitrogen to gold. Since the orbital of the electron lone pair is orthogonal and not part of the aromatic backbone of the molecule we do not expect any influence of the furan rings on the binding properties of BDF_{NN}.

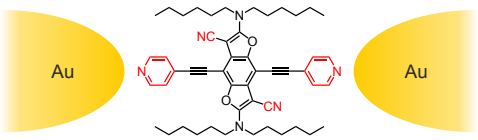

Figure 2.8: Possible binding sites (red) of the BDF_{NN} molecule on gold electrodes.

The two conductance intervals in Fig. 2.7 points to different binding sites of the molecule. Beside the pyridyl ends, the cyanide (or nitrile) groups of the furan rings can form a bond to gold. Figure 2.8 shows possible molecular anchors to the gold electrodes. We will discuss the binding sites in more detail for BDF_{SS}.

2.3.2 Benzodifuran-dithiol (BDF_{SS})

The thiolated benzodifuran molecule is on both ends protected by acetylene groups. The deprotection of these end groups by tetrabutyl ammonium hydroxide (TBAH) were tested via thin layer chromatography (TLC). Here, the molecule was dissolved in dichloromethane/cyclohexane (1:1 v/v). During the measurements argon gas was bubbled through the liquid cell in order to prevent oxygen reacting with the sulphur ends and finally polymerizing the BDF_{SS} molecule. The concentration of TBAH was stepwise increased after each measurement series.

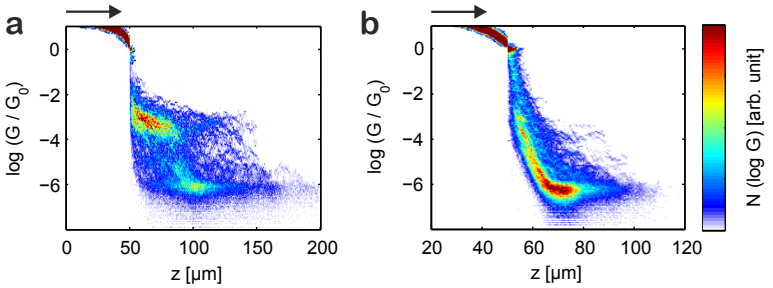

Figure 2.9: 2D histograms of **(a)** 200 and **(b)** 400 consecutive opening traces as examples. We used **(a)** THF/mesitylene and **(b)** dichloromethane as solvents. In both cases the concentration was c(BDF_{SS}) = 250 µM. The TBAH concentration c(TBAH) was **(a)** 67 µM and **(b)** 467 µM, and the push rod speed was set to 31.2 µm/s. **(a)** The histogram contains a clear plateau region in the interval $G = (10^{-4}...10^{-3})\ G_0$ whereas the right histogram **(b)** contains not such a region.

Figure 2.9 shows 2D histograms of opening traces for two different solvents. The measurement in dichloromethane (Fig. 2.9b) has no distinct region of conductance plateaus although some of the individual traces contain plateaus. In contrary, the other 2D histogram (Fig. 2.9a) has a clear plateau concentration in the conductance interval between $10^{-4}\ G_0$ and $10^{-3}\ G_0$. In order to gain more insight we first sorted traces into two groups, similar we did for the pyridyl-terminated molecule. 77 % of all traces contain a conductance plateau (in THF/mesitylene). In dichloromethane we can also find plateaus, but less frequent and at considerably higher deprotection (or c(TBAH)). In Fig. 2.10 are the 1D histograms of traces with (Fig. 2.10c) and without (Fig. 2.10a) plateaus presented. The histogram of traces with plateaus shows a clear peak which can be fitted by a Gaussian function ($3.6 \cdot 10^{-4}\ G_0$) [30]. A minor peak is visible at around $10^{-5}\ G_0$. The conductance peak of thiolated oligo(phenylene ethynylene) (OPE_{SS}) is with $2.3 \cdot 10^{-4}\ G_0$ at

U_{bias} = 0.1 V slightly lower [27].

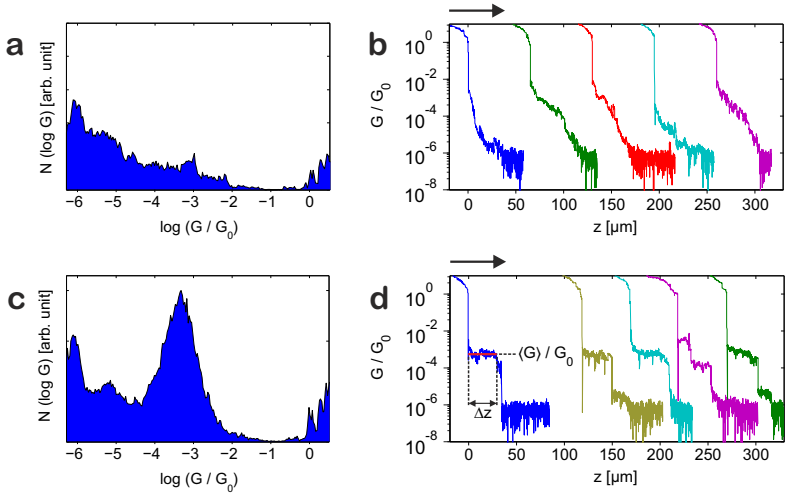

Figure 2.10: **(a,c)** 1D logarithmic histograms of conductance values. **(a,b)** All 154 opening traces have no visible plateau. **(c,d)** 46 opening traces contain conductance plateaus. **(b,d)** Typical measured opening traces as examples. The concentrations of BDF_{SS} and the deprotecting agent TBAH in THF/mesitylene were 250 µM and 67 µM, respectively. The push rod speed was set to 31.2 µm/s. The histogram with plateaus **(c)** shows a very pronounced peak in the interval $(10^{-4}...10^{-3})$ G_0. We obtained the peak value of $3.6 \cdot 10^{-4}$ G_0 by a Gaussian fit. A minor peak is visible at approximately 10^{-5} G_0. We studied the distribution of individual plateaus, and determined their length ($\triangle z$) and average conductance ($\langle G \rangle / G_0$) **(d)**.

We had a closer look at the plateaus of individual traces. The length ($\triangle z$) and average conductance value ($\langle G \rangle / G_0$) of plateaus were estimated like it is illustrated in Fig. 2.10d. A plot of the length vs. the average conductance in Fig. 2.11 makes the distribution of plateaus clearer. Two conductance intervals are marked in this diagram. Almost two third (61 %) of all plateaus are in the logarithmic interval ($\log_{10}(\langle G \rangle / G_0)$ = -3.9...-2.7) whereas only one quarter (24 %) are in the interval ($\log_{10}(\langle G \rangle / G_0)$ = -5.7...-4.7). A typical length of these plateaus (50 µm) would correspond to an electrode separation of 0.8–2 nm [28].

We explain the two conductance ranges with different binding sites of the molecule (see Fig. 2.12). The opening traces of the pyridyl-terminated molecule

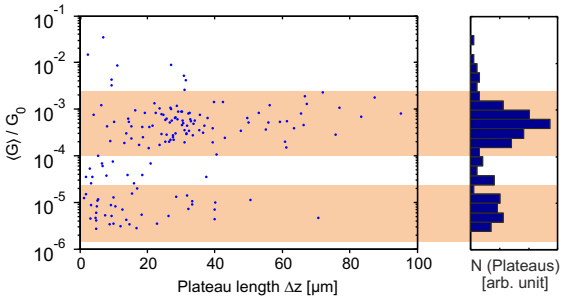

Figure 2.11: Plateau statistics of 154 opening traces and (right) histogram of conductance plateaus. The concentrations in THF/mesitylene were c(BDF_{SS}) = 250 µM and c(TBAH) = 67 µM. We see two main intervals where the plateaus are located. In the lower interval ($\log_{10}(\langle G\rangle/G_0)$ = -5.7...-4.7) are 24 % and the upper interval ($\log_{10}(\langle G\rangle/G_0)$ = -3.9...-2.7) contains 61 % of all plateaus.

do not contain any plateaus longer than 5 µm. By contast, the BDF_{SS} molecule has in two conductance intervals long plateaus. We think that in the electrode binding represented by both intervals are thiol groups involved. The molecule contains two cyanide groups located at the furan rings. These cyanide groups are sterically close to the thiol ends so that nitrogen can anchor at the gold electrodes [27]. Additional binding of the central benzene ring laying flat on the electrodes might be possible as well. The high conductance range would correspond to a Au-S-BDF_{SS}-S-Au configuration whereas the low range is the Au-N-BDF_{SS}-S-Au binding.

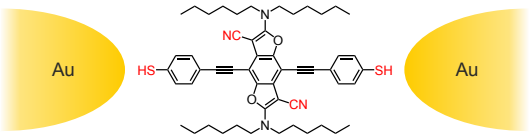

Figure 2.12: Possible binding sites (red) of the deprotected BDF_{SS} molecule on gold electrodes.

The two conductance ranges can also be illustrated by a cruciform structured molecule containing thiol and pyridyl anchors [31, 32]. If the thiol group is still deprotected two conductance peaks were observed which points to a pyridyl-Au and AcS-Au binding. Similar to BDF_{NN} we do not expect a weakening of the

thiol-Au binding due to the furan side groups [29, 33].

2.4 Summary

We studied a pyridyl- and thiol-terminated derivative of benzodifuran (BDF_{NN} and BDF_{SS}) in a mechanically controllable break junction. The opening traces of BDF_{SS} contain long plateaus in the order of 50 µm, whereas the plateaus of BDF_{NN} are very short with less than 5 µm. In order to gain more insight we studied the statistical distribution of the conductance plateaus, and found two main intervals. For BDF_{SS} the upper interval ($\log_{10}(\langle G \rangle / G_0)$ = -3.9. . .-2.7) contains 61 % and the lower interval ($\log_{10}(\langle G \rangle / G_0)$ = -5.7. . .-4.7) 24 % of all plateaus. Both intervals indicate that the thiol ends as well as the cyanide groups can bind to gold. The higher conductance interval would correspond to a Au-S-BDF_{SS}-S-Au bridging and its average conductance value is fitted to be $3.6 \cdot 10^{-4}\, G_0$. We do not expect that the central furan rings alter the binding strength of both molecules to the gold electrodes.

CHAPTER 3

PHOTOLUMINESCENCE MEASUREMENTS – BASIC ASPECTS

We performed photoluminescence (PL) measurements with a confocal Raman microscope using two lasers as coherent light sources. Here, we focus on general aspects of measurements on gold nanostructures.

In this chapter we want to discuss the fundamental mechanism of gold photoluminescence. And we compare the photoluminescence of a film with that of an isolated nanostructure. Finally, we focus on general issues like incident laser power or temporal stability of the spectrum which we need to know for all systematic studies in chapters 4 and 5.

3.1 Nanoscale Antennas

Fabrication

The fabrication was done by electron-beam lithography and a standard metallization process. The antenna structures were written onto a thermally oxidized silicon wafer whose oxide layer is approximately 400 nm thick. The antennas were designed to be separated by 4–6 µm from each other. After the development of the resist 50 nm of gold were deposited with an adhesion layer of 0.5 nm titanium. The adhesion layer has a damping effect on the plasmonic behaviour [34] therefore we keep that layer as thin as possible.

In order to decrease the gap size within a dipole antenna we evaporated the gold from different angular directions. Thus gaps below 10 nm are possible under a free-standing PMMA bridge. One example is given in Fig. 3.1.

Before each measurement we removed on average 5 nm gold by an argon

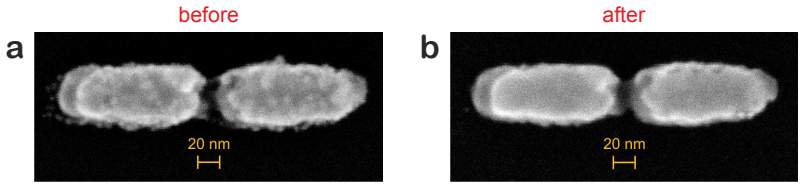

Figure 3.1: Comparison of the same nanostructure before **(a)** and after **(b)** an argon plasma etching. The nanostructure was fabricated by angular metal deposition which leads to gold steps at the tails. During etching small and isolated gold clusters were removed and the gold surface itself smoothened.

plasma (Fig. 3.1). In this process we can remove small gold clusters around the antenna which could disturb its plasmonic response. Additionally, the antenna surface becomes smoother. Details of the fabrication process can be found in appendix A.

Measurement on Raman Microscope

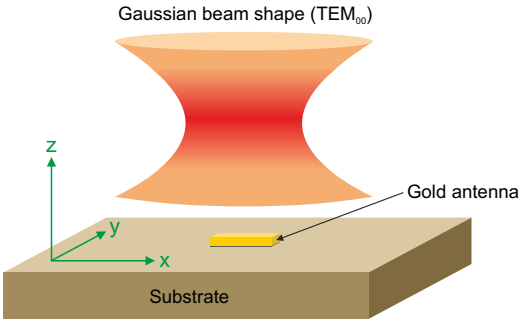

Figure 3.2: Illustration of the laser beam focused close to a nanostructure. The Cartesian coordinates x, y and z indicate the position of the focus relative to the nanostructure.

Optical measurements are performed on a confocal Raman microscope from the company WITec (Germany). As light sources there are two lasers coupled into the microscope, a Nd:YAG and HeNe laser with a wavelength of $\lambda_0 \approx 532\,\text{nm}$ and

633 nm, respectively. We measured at room temperature in ambient atmosphere. In Fig. 3.2 the coordinate system of the measurements is illustrated. We define the position of the laser focus relative to the illuminated nanostructure, in which the origin ($x = y = z = 0$) corresponds to the point of maximum photoluminescence. Hence, moving the focus in $+z$-direction means that we increase the distance between the nanostructure and objective.

Edges of the CCD sensor chip are not homogeneously illuminated by the light which is coupled into the spectrometer. This effect is caused by the spectrometer optics itself and is known as vignetting in the photography. We measured this effect on the instrument in order to normalize each spectrum (see appendix C). Furthermore spectra are normalized by the quantum efficiency (QE) of the CCD chip, by the measuring time [s] and the laser power [mW]. From each spectrum a background is subtracted which includes the dark current of the CCD chip inside the spectrometer.

Analysis

We extracted the geometry of the nanostructures from high-resolution SEM images. The length (a) and width (b) is determined by drawing a box around an antenna. The script which does it automatically is listed in appendix D.

From the measured spectrum (I) either a silicon spectrum I_{Si} or the spectrum without any laser excitation I_0 is subtracted. The resulting spectrum of an antenna is fitted by a Lorentzian peak function in order to evaluate the amplitude I_{max}, the position E_{max} and the full width at half maximum (FWHM) E_{FWHM}. More information can be found in appendix D.

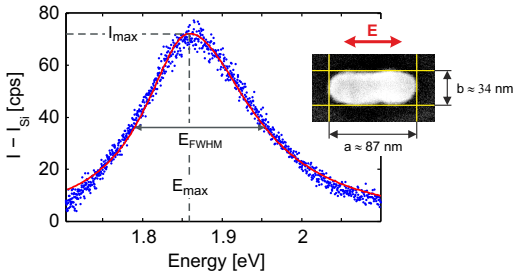

Figure 3.3: Gold PL spectrum of a nanostructure (inset) at $\lambda_0 = 532$ nm (2.33 eV) and $P \approx 500\,\mu$W. The incident light was polarized parallel to the long axis of the nanostructure. The spectrum is fitted by an asymmetric Lorentzian peak function in order to extract the amplitude I_{max}, the peak position E_{max} and the FWHM of the peak E_{FWHM}.

3.2 Fluorescent Dye Molecules on Nanostructures

Fluorescent dye molecules in the presence of metallic nanostructures can lead to an enhanced fluorescence of the molecule [35–37]. The reason is that absorption and emission process are altered by the plasmon of the nanostructure. One example of a fluorescent dye molecule would be the benzodifuran derivatives (Fig. 2.1) whose electrical properties are measured in chapter 2. We used the fluorescent dye molecule "Fluorescent Red 633" (Fluka) in order to test our nanoscale antennas. This dye molecule (Fig. 3.4) has in ethanol an absorption and emission maximum at 637 nm and 657 nm, respectively, and is therefore well suited for the excitation by a HeNe laser.

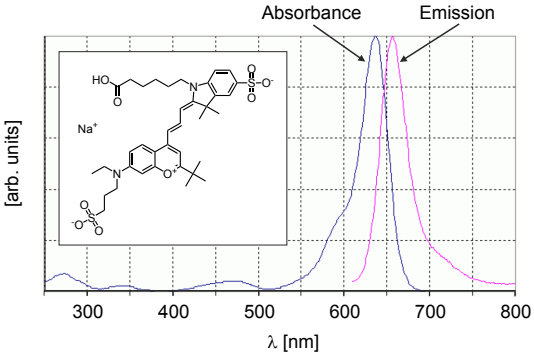

Figure 3.4: Absorption and emission spectrum of the molecule "Fluorescent Red 633" (Fluka) [38]. The inset shows its chemical structure.

We spin coated the dye molecule onto the sample with the antenna structures (3000 rpm, 40 s). Here, the molecule was dissolved in ethanol (200 µM) and the sample was etched in an argon plasma before. Between measurements the sample was stored in a cool place under argon to prevent the molecule from any kind of aging.

3.2.1 Reducing the Molecular Bleaching

The dye molecule we used is sensitive to an oxygen containing atmosphere. Therefore we developed a cell (Fig. 3.5) which is mounted on the microscope stage. This cell has a gas inlet and outlet. The gas connection to argon allows an inert gas atmosphere inside the cell which contains the sample.

Figure 3.6 illustrates the difference of measurements in air and an oxygen-free

environment. We detected a much higher fluorescence intensity in argon and the fluorescence itself is decaying in air a lot faster.

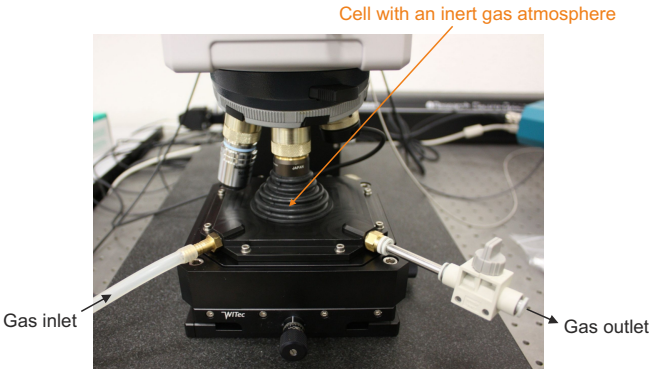

Figure 3.5: Photo of a mounted cell on the microscope stage which encapsulates a sample into an oxygen-free atmosphere.

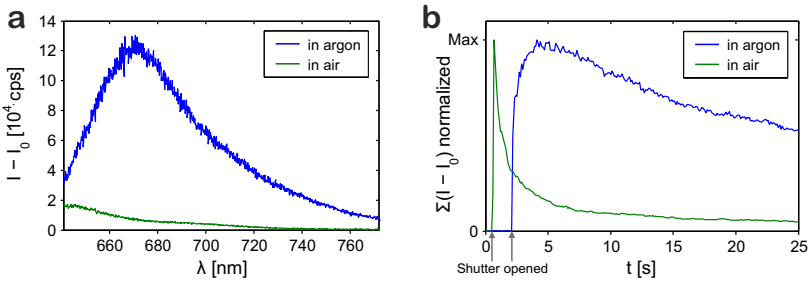

Figure 3.6: **(a)** Fluorescence spectra of the dye molecule at $P = 10\,\mu W$ and an integration time of circa 1 s. The spectrum in argon shows a significantly higher intensity. **(b)** Time-dependent fluorescence decay of the integrated spectra ($P = 10\,\mu W$). The fluorescence measured in air decays much faster than in argon.

3.2.2 Mapping the Photoluminescence

First measurements were done in air at the ETH Zürich. Then we tested the fluorescence on a substrate with nanostructures in argon atmosphere. The molecules were spin coated onto the substrate and were therefore uniformly distributed over the surface. We see a uniform fluorescence signal as a result of excitation by the HeNe laser (λ_0 = 633 nm), beside the position where nanostructures are located (Fig. 3.7). Here, the molecular fluorescence is enhanced. The enhancement can basically be described by a factor $f_{Enhancement}$ which is the difference in intensity on nanostructures I_F and the uniform background signal $I_{F,0}$ normalized by the background [37].

$$f_{Enhancement} = \frac{I_F - I_{F,0}}{I_{F,0}} \tag{3.1}$$

We use the integrated value of a spectrum as the fluorescence signal I_F (Fig. 3.7b):

$$I_F = \sum_{Spectrum} I - I_0$$

In Fig. 3.7c is the enhancement factor $f_{Enhancement}$ shown in 200 nm steps around a nanoantenna. The background fluorescence $I_{F,0}$ is the averaged signal I_F of the edge pixels in this plot. The fluorescence is more than 70 % enhanced on the position of the fabricated nanoantennas. This demonstrates that the near-field of the nanostructure alters the absorption and emission process of the dye molecule.

It is interesting to note that in the dark-field image of Fig. 3.7b the antenna structures appear in a specific colour. From the colour in those dark-field images we can estimate the geometry of the antenna, e.g. distinguish between monopole and dipole antennas. This effect was discussed in [39] for silver nanoparticles.

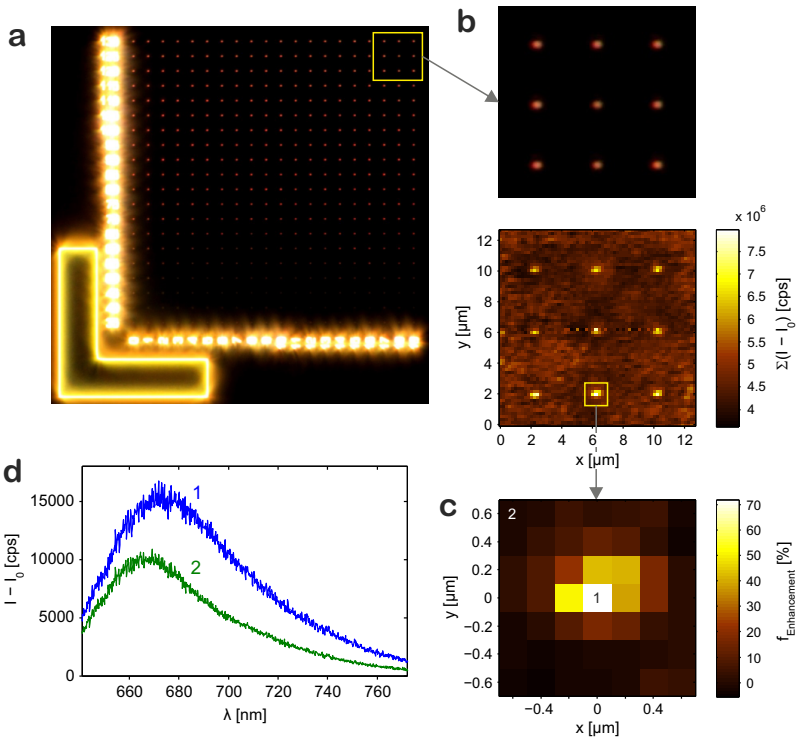

Figure 3.7: **(a)** Dark-field image of a nanoantenna array. The nanostructures, here visible as reddish spots, are separated by 4 µm. **(b)** Zoom-in of the dark-field image with 3×3 antennas and below the same area with the molecular fluorescence in an argon atmosphere. The dye molecule was spin coated onto the substrate before. The fluorescence was measured in 200 nm steps and a dwell time of 37 ms per pixel and spectrum. The laser power was set to 1 mW. Here, the sum over the whole spectrum is presented. **(c)** Zoom in around one nanostructure marked in **(b)**. Here, the integrated spectra are presented as enhancements relative to the edge pixels as background (Eq. 3.1). Two example spectra indicated with 1 and 2 are shown in **(d)**.

3.3 Gold Photoluminescence

3.3.1 Scaling Effects

Photoluminescence of noble metals like copper and gold was first observed by A. Mooradian [40]. He explained this process by an electron excitation from the upper d-bands into the sp-conduction band above the Fermi surface (Fig. 3.8b). If the exciting light is below the photon energy of approximately 2.4 eV (λ = 516 nm), then only interband transitions near the X symmetry point are involved. The electrons in the conduction band relax and can eventually recombine with a d-band hole by emitting a photon.

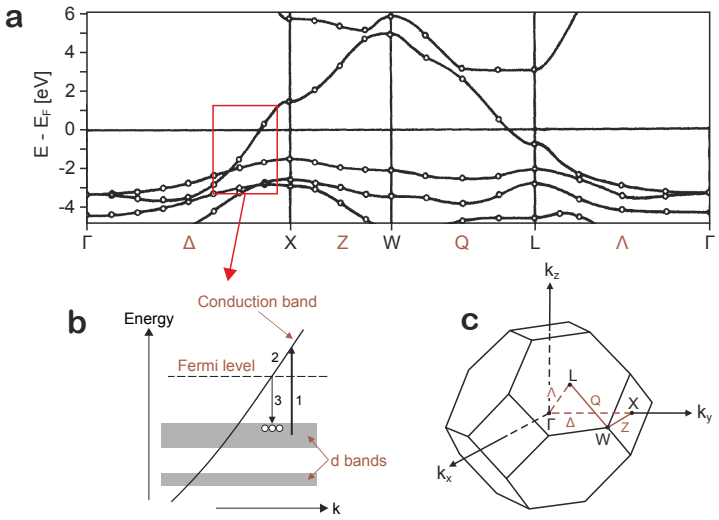

Figure 3.8: (a) Relativistic energy bands of gold adapted from [41]. The red marked area is schematically shown in **(b)**. Here, the gold photoluminescence is explained by excitation (1) of an electron from the upper d-bands into the sp-conduction band, relaxation (2) and radiative electron-hole recombintaion (3). **(c)** Brillouin zone including symmetry points of a fcc crystal.

Luminescence of a Gold Film

We measured the intrinsic photoluminescence of gold on a 45 nm thin film. The film was plasma etched before the measurement which reduces the surface

roughness (see Fig. 3.1). In Fig. 3.9 are the PL spectra shown with an excitation at λ_0 = 532 nm (2.33 eV) and λ_0 = 633 nm (1.96 eV). Each spectrum contains a maximum close to the light excitation, decays rapidly and reaches zero between 1.6 and 1.7 eV. For λ_0 = 532 nm we collect 6–7$\times$ more intensity at the maximum than for λ_0 = 633 nm.

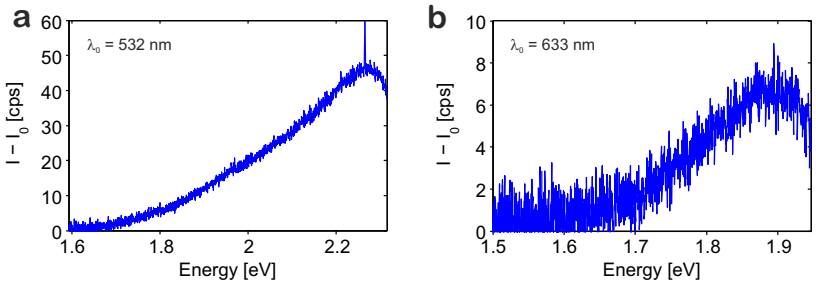

Figure 3.9: Comparison of the photoluminescence of a 45 nm gold film at **(a)** λ_0 = 532 nm (2.33 eV) and **(b)** λ_0 = 633 nm (1.96 eV). The laser power was set to 1 mW.

Luminescence of a Gold Nanostructure

As the next step we measured the gold photoluminescence of a nanostructure. The thickness (45 nm) is the same like for the flat gold film in order to compare their luminescence. Both structures are fabricated in the same process and should have a similar surface morphology. In Fig. 3.10 the PL spectrum of a monopole antenna is presented together with that of a gold film. By comparing the maximum intensities one can find an approximately 40$\times$ higher fluorescence for the gold nanostructure. This ratio is even higher if the illuminated area is considered. If one assumes a circular spot onto the film according to the Rayleigh criterion ($d = 0.61\lambda/NA \approx 429$ nm) and the nanostructure dimension of $a \times b$ = 96 nm $\times$ 37 nm, then the intensity ratio is almost 1700. We want to further discuss the origin of this huge enhancement in section 4.1.2.

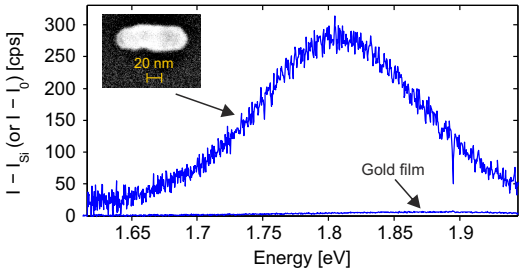

Figure 3.10: Comparison of the gold photoluminescence of film and nanostructure of the same thickness (45 nm). The excitation wavelength was λ_0 = 633 nm. The laser power was 100 µW and 1 mW for the nanostructure and the thin film, respectively.

3.3.2 Spatial Mapping

It is very important to focus the Gaussian beam of the laser microscope [42] onto the nanostructure. Changing one of the spatial coordinates (x, y, z) can easily halve the signal (Fig. 3.11a). Therefore one has to exercise care about maximizing the PL signal in all three dimensions. The main part of the measurement error is due to a defocus which we estimated at 10 %. A summary of all measurement errors is listed in appendix B.

We first perform a 2D scan in the z-plane for localization of the nanostructure. With its help we can further maximize the PL signal by slowly shifting the position of the confocal beam relative to the gold structure.

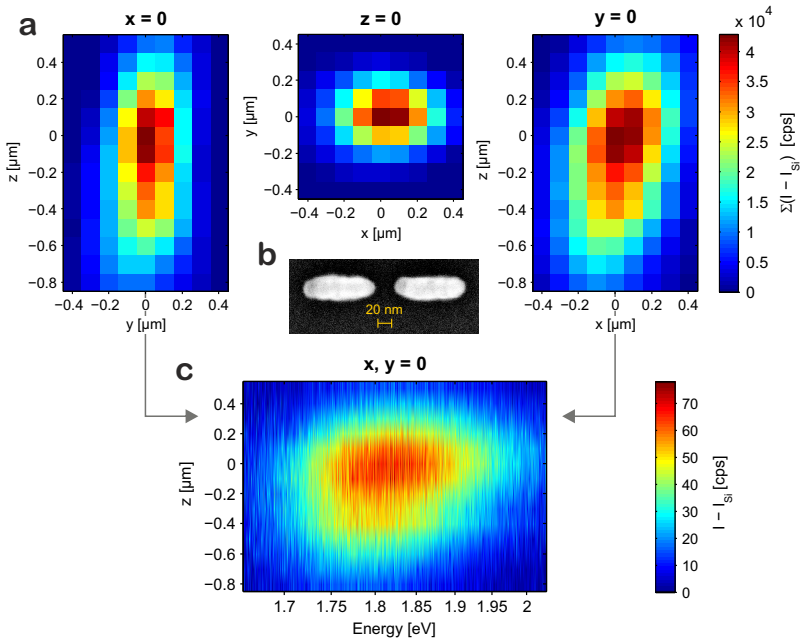

Figure 3.11: Three-dimensional mapping of the gold photoluminescence of a dipole antenna (λ_0 = 532 nm and P = 1 mW). **(a)** Integrated spectra dependent on the spatial coordinates (x, y, z). Three cross sections are shown where one coordinate is fixed to 0. The position of maximum luminescence is at the point of origin (x, y, z = 0). In the section y = 0 is a small drift in x-direction during the scan visible. **(b)** SEM image of the measured dipole antenna. **(c)** PL spectra dependence on the z-position (x, y = 0).

3.3.3 Aspects of the Laser Intensity

In this section we want to discuss the implication of the incident laser intensity on the illuminated nanostructures.

Dependence of the Photoluminescence on the Laser Intensity

In Fig. 3.12a is the power dependence of the PL signal presented. The dipole antenna emits light which is before the power normalization proportional to the incident laser power itself. The line $P \propto I$ (red) is well fitting the data points. Therefore it is very reasonable to normalize experimental results by the laser power in order to get comparable results in units [cps] (see appendix C). The normalized spectra in Fig. 3.12b overlap well and in particular the shape is conserved. Therefore, we can assume I_{max}, E_{max} and E_{FWHM} to be independent of the incident laser power.

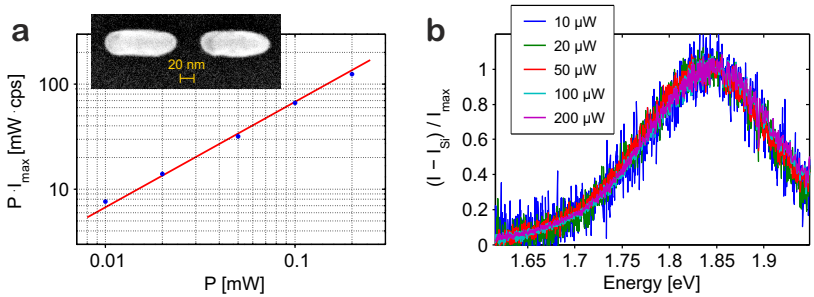

Figure 3.12: Power dependence of a single antenna (λ_0 = 633 nm). **(a)** PL intensity before normalization by the laser power vs. the power itself. The red line shows the proportionality as an evidence of the single-photon photoluminescence. The inset is an SEM image of the illuminated antenna. **(b)** Normalized spectra measured at different laser powers. The shape of the spectra overlaps well and can be assumed to be independent of the power.

Temporal Stability of the Spectrum

An important issue is the stability of the luminescence during the measurement. We want to ensure that the final spectral parameters (I_{max}, E_{max} and E_{FWHM}) are stable in time. The spectrum in Fig. 3.13a is very stable over almost 30 s of illumination. On the right (Fig. 3.13c) the spectral parameters are shown which

we received from Lorentzian fits at each time. The error of the amplitude (I_{max}) is not shown since the measurement error is dominated by other sources, e.g. defocus.

Before each measurement we proved the stability of the PL signal by such a temporal scan. Irreversible damage on the gold nanostructure due to the illumination would appear immediately in the recorded spectrum (see next section). We accumulated at least 100 spectra (t = 212 ms) in order to smooth the final result. This leads to a total measuring time per spectrum of at least 21 s.

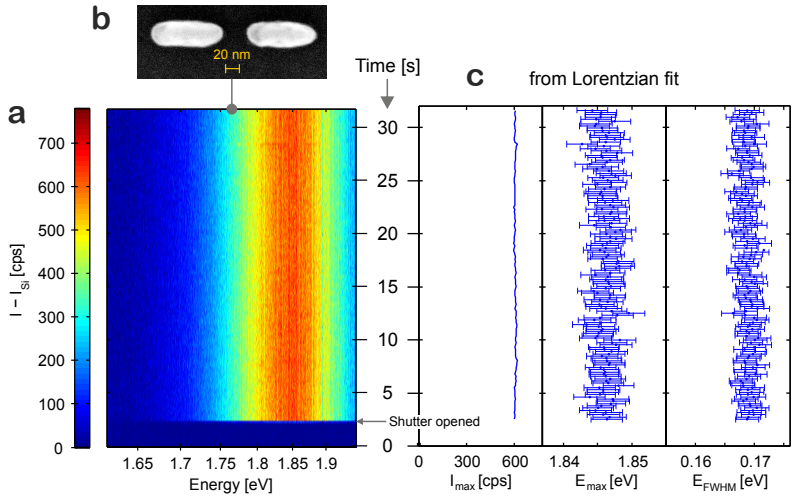

Figure 3.13: Temporal stability of the gold luminescence during the measurement (λ_0 = 633 nm and $P \approx 200\,\mu W$). **(a)** Time-dependent spectra show over almost 30 s a stable spectrum. **(b)** SEM image of the measured dipole antenna. **(c)** Lorentzian fit of each spectrum vs. time.

Damage Thresholds

If the incident laser power is too high or the exposure time on a nanostructure too long, then we can see an irreversible change in the PL spectrum (Fig. 3.14). Deformation of gold nanostructures upon irradiation was in detail studied by A. Kuhlicke *et al.* [43] and S.-S. Chang *et al.* [44].

We measured a dipole antenna at the power of P = 1 mW for several minutes. In Fig. 3.14 is clearly visible that the intensity is changing more than one order of

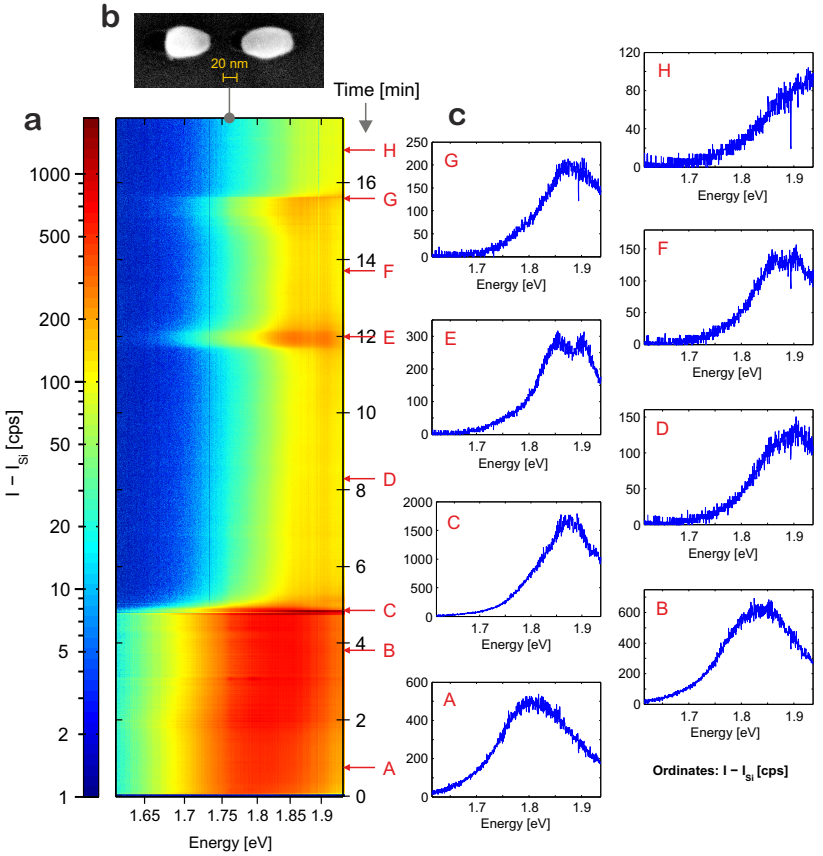

Figure 3.14: Damage of the nanoscale gold structure due to irradiation (λ_0 = 633 nm and $P \approx 1$ mW). **(a)** Time-dependent spectra in a logarithmic scale over several minutes. The PL spectrum changes by more than an order of magnitude. **(b)** SEM image of the imaged dipole antenna after the measurement. Both antenna arms show a significant deformation where the shape becomes rounder and the aspect ratio is reduced. **(c)** Selected spectra at different times are represented. The time is marked on the corresponding scale in **(a)**.

magnitude. The major trend is that the maximum in the spectra shifts towards higher energy values which would correspond to a reduction of the aspect ratio [44]. In the SEM image (Fig. 3.14b) the structure looks significantly rounded shaped compared to the undamaged nanostructure in Fig. 3.13b. We assume that the gold is molten upon the intensive focused light. It forms a more spherical shape with a lower surface-to-volume ratio in order to reduce the surface tension. On other nanostructures we also observed an explosion which leads to small gold clusters spread around.

In our measurements we are keeping the time of irradiation as short as possible to avoid any damage. The laser power is chosen as low as possible with a sufficient signal-to-noise ratio. We used on gold nanostructures of a normal shape usually laser powers of 500 µW (λ_0 = 532 nm) and 100 µW (λ_0 = 633 nm).

3.3.4 Aspects of the Laser Polarization

Figure 3.15 shows the polarization dependence on the luminescence. The electric field vector is rotated by a half-wave plate relative to the long axis of the monopole antenna. We see a maximum photoluminescence when the electric field is polarized parallel to the long axis (α = 0) and the minimum when the light is polarized perpendicular ($\alpha = \pm 90°$). We observe the same dependence for dipole antennas.

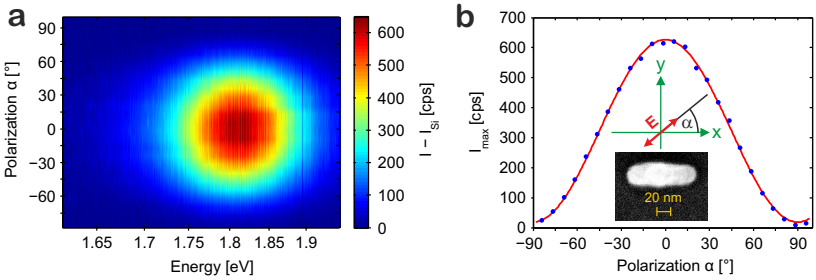

Figure 3.15: Dependence of the gold luminescence on the incident light polarization. **(a)** PL spectra dependent on the polarization angle relative to the long antenna axis. **(b)** Peak amplitude (I_{max}) dependence on the polarization angle. The red line is a fit ($a \cdot cos^2(\alpha) + b$). The inset is an SEM image of the measured antenna.

The $I_{max}(\alpha)$-dependence can be fitted by a ($a \cdot cos^2(\alpha) + b$) function (Fig. 3.15b) which can be derived by the vector elements of the polarizability along the principal

axes. In our measurements we always optimized α so that we could detect a maximum of signal.

3.4 Summary

We fabricated nanoscale antennas on an oxidized silicon wafer. The antennas were tested by measuring the molecular fluorescence on the substrate. Here, a dye molecule was spin coated before onto the substrate. As a result, we see an enhanced fluorescence at the positions of the nanostructures.

We measured the intrinsic luminescence of gold on a thin film and compared it with that of a nanostructure. Afterward we discussed general aspects of optical measurements. The three-dimensional focusing on the nanostructure is essential to receive a sufficient signal. It is important to choose the appropriate laser power. It has to be high enough for a good signal-to-noise ratio but not too high that irreversible damage on the nanostructure is expected. By changing the light polarization we can see the directionality of the photoluminescence. In our measurements we always aligned the polarization along the long axis of the nanostructure.

CHAPTER 4

PHOTOLUMINESCENCE OF GOLD NANOSTRUCTURES – MONOPOLES

Gold nanostructures are an important object for plasmonic applications. In this chapter we want to discuss their photoluminescence (PL) properties and especially focus on the size dependence of the luminescence spectra.

4.1 Size Dependence

4.1.1 Experimental Results

We studied the photoluminescence of gold monopole antennas at different wavelengths (λ_0). The laser polarization was aligned along the long antenna axes. In Fig. 4.2 we show the length dependence of the luminescence at λ_0 = 532 nm. The intensity I_{max} reaches a maximum at around a_{SEM} = 90 nm (Fig. 4.2a). The peak position E_{max} (Fig. 4.2b) follows a redshift from short to long antennas which seems to saturate at approximately 1.7 eV.

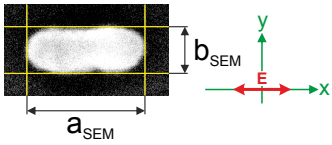

Figure 4.1: Length (a_{SEM}) and width (b_{SEM}) of a monopole antenna are taken from a SEM image.

The measured spectra were fitted to a Lorentzian peak function in order to extract the values for I_{max}, E_{max} and E_{FWHM}. For long monopoles (Fig. 4.2c, coloured area) we detected broad PL peaks with a non-Lorentzian shape. This makes it impossible to determine E_{max} from a Lorentzian fit. We will discuss this effect in section 4.2.

We studied the same antennas at a different excitation wavelength (λ_0 = 633 nm) and observed a similar trend for the intensity of the spectra (Fig. 4.3a). Here, the maximum of I_{max} is also located around a_{SEM} = 90 nm. The energy peak position follows a redshift towards longer antennas until we measure spectra different from Lorentzian shape (Fig. 4.3c). In the coloured area the spectra become broader the longer the monopole is, similar to the behaviour at a λ_0 = 532 nm illumination. The increase of the energy E_{max} towards shorter monopoles is less pronounced at λ_0 = 633 nm.

L. Novotny [45] discussed the scaling of metallic antennas in the optical regime. The simple scaling of an ideal half-wave antenna ($a = \lambda_0/2$) breaks down since the electromagnetic wave is penetrating into the metal and is therefore no longer perfectly reflected. Hence, it is necessary to substitute λ_0 by a shorter effective wavelength λ_{eff}, which scales linearly to the incident wavelength $\lambda_{eff} = n_1 + n_2[\lambda/\lambda_p]$. Here, n_1 and n_2 (> 0) are coefficients and λ_p = 138 nm is the plasma wavelength of gold. The new condition for half-wave antennas (with $a = \lambda_{eff}/2$) explains the redshift (E_{max}) for longer monopoles in Figs. 4.2b and 4.3b. The maximum for I_{max} ($a \approx 90$ nm) would mean that λ_{eff} of the corresponding excitation wavelength λ_0 (532 and 633 nm) matches the half-wave condition (see Figs. 4.2a and 4.3a).

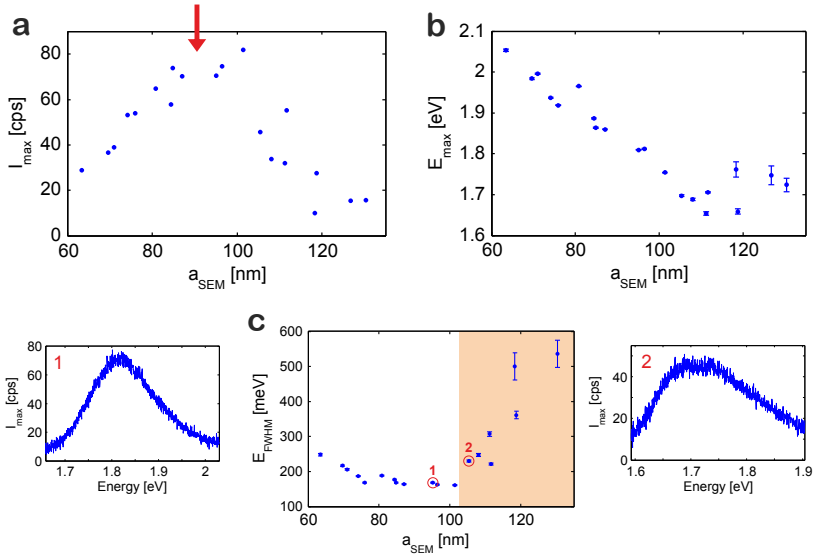

Figure 4.2: Length dependence of monopole antennas with width b_{SEM} = 35 ± 2 nm. The laser wavelength and power were λ_0 = 532 nm and $P \approx$ 500 µW, respectively. **(a)** Intensity of the gold luminescence. The arrow marks a maximum around a_{SEM} = 90 nm. **(b)** Position of the PL peak. It shows a blue-shift towards shorter antennas. **(c)** FWHM of the PL peak with two example spectra. In the orange shaded area the peak significantly broadens and differs from Lorentzian shape. This leads to an imprecise evaluation of the peak position in **(b)**.

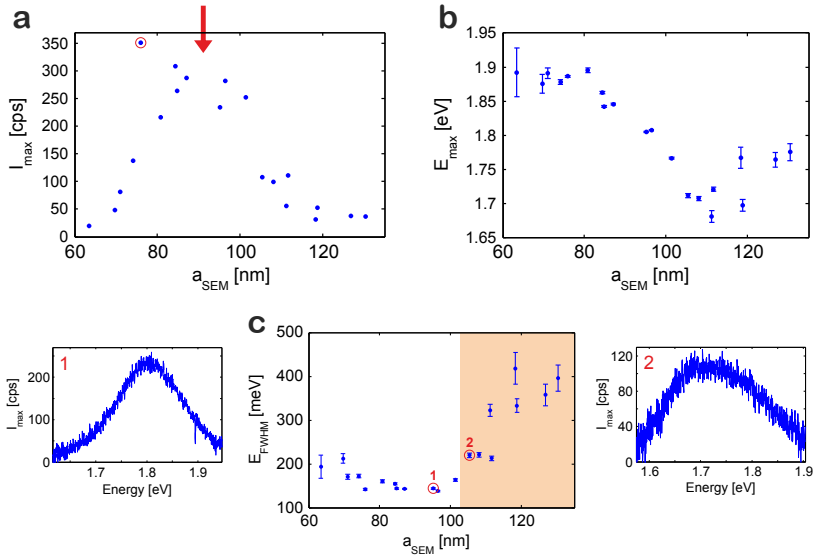

Figure 4.3: Length dependence of the same monopole antennas as in Fig. 4.2. The laser wavelength and power were λ_0 = 633 nm and $P \approx 100\,\mu$W, respectively. **(a)** Intensity of the gold luminescence. The arrow marks a maximum around a_{SEM} = 90 nm. The red encircled data point is an outlier which can be due to nanoscopic shape variations. **(b)** Position of the PL peak. It shows a blue-shift towards shorter antennas but less pronounced than for λ_0 = 532 nm. **(c)** FWHM of the PL peak with two example spectra. In the orange shaded area the peak significantly broadens and differs from Lorentzian shape. This leads to an imprecise evaluation of the peak position in **(b)**.

4.1.2 Gold Photoluminescence enhanced by Plasmons

The enhancement of an electrical field on rough surfaces is described by hemisperoids [46, 47]. Here, hemispheroids are a model for surface protrusions sitting on a flat perfectly conductive metal surface. Inside these surface protrusions collective electron movements, known as plasmons, can be excited by an incident electric field $\vec{E}_0$. The plasmon creates a local electric field $\vec{E}_{loc}$ around the hemispheroids which is highly enhanced. To describe the relationship between the incident and local field one can introduce a macroscopic local-field correction factor $\overleftrightarrow{L}(\omega)$ [48]. The local electric field is calculated by $\vec{E}_{loc} = \overleftrightarrow{L}(\omega) \cdot \vec{E}_0$. E. Dulkeith *et al.* [49] discuss the enhanced PL process by a radiative decay of the particle plasmon [50].

G. T. Boyd *et al.* [51] applied the model of hemisperoids to determine the photoluminescence of rough gold surface. This model was later used to describe quantitatively the luminescence of gold nanorods [52, 53]. The shape of a nanorod is approximated to be a spheroid (see Fig. 4.4).

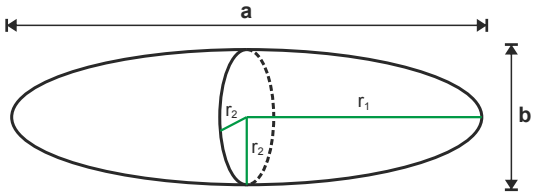

Figure 4.4: Spheroid (length a and width b) as a model for monopole antennas.

Here, the depolarization factor A and the lightning-rod factor $L_{LR}(a/b) = A^{-1}$ are defined as:

$$L_{LR} = 1 - \frac{\xi Q_1'(\xi)}{Q_1(\xi)}$$

$$\xi = \frac{1}{\sqrt{1 - \left(\frac{b}{a}\right)^2}}$$

$$Q_1(\xi) = \frac{1}{2}\xi \ln\left(\frac{\xi + 1}{\xi - 1}\right) - 1$$

$$Q_1'(\xi) = \frac{dQ_1(\xi)}{d\xi}$$

$L_{LR}(a/b)$ is a purely geometric factor depending only on the aspect ratio a/b of

the spheroid or the nanorod. The local-field correction factor L is then defined by:

$$L(\omega) = \frac{L_{LR}}{\frac{\epsilon(\omega)}{\epsilon_m} - 1 + L_{LR}\left(1 + \frac{4}{3}\pi^2 i \cdot \frac{V}{\lambda^3} \cdot (1 - \epsilon(\omega))\sqrt{\epsilon_m}\right)} \tag{4.1}$$

It depends on the frequency ω or the wavelength λ of the light. $\epsilon(\omega)$ is the dielectric function of gold which were taken from [54]. Other parameters are the dielectric constant of the surrounding medium ϵ_m and the volume of the spheroid $V = \frac{1}{6}\pi ab^2$. Then the single-photon PL power calculates as:

$$P_1 = 16\beta_1 |E_0|^2 \cdot V |L^2(\omega_{exc}) L^2(\omega_{em}))| \tag{4.2}$$

Here β_1 is a constant including the intrinsic PL spectrum of gold and E_0 is the incident electric field. ω_{exc} and ω_{em} are the excitation and emission frequency, respectively.

From Eq. 4.2 follows that the PL power P_1 is proportional to the incident light intensity ($\propto |E_0|^2$). This ensures that we measure the single-photon luminescence of gold antennas (see section 3.3.3). Apart from that, other groups measured two-photon or even four-photon luminescence with a fs-pulsed laser excitation of the gold nanostructure [55–58].

4.1.3 Conclusions from the Model

For a certain incident electric field E_0 and excitation frequency ω_{exc} in Eq. 4.2 the PL spectrum $P_1(\omega_{em})$ is proportional to:

$$P_1(\omega_{em}, a, b, \epsilon_m) \propto |L^2(\omega_{em}, a, b, \epsilon_m)| \tag{4.3}$$

We want to describe the measured PL spectrum by this model. Therefore we fitted the normalized spectrum to a normalized model function $P_1(\omega_{em})$ with $E_{em} = \hbar\omega_{em}$. Geometrical dimensions a and b of the antenna are taken directly from SEM images. The free fitted parameter is the complex dielectric constant ϵ_m of the environment. In the fit we excluded data points < 1.73 eV (interband absorption edge, see section 4.2) and > 2.18 eV (gold film, see section 3.3.1). The model function matches very well the normalized spectra in Fig. 4.5 with $\epsilon_m \approx 2.1$–2.2.

The antenna is placed at the interface of air/SiO_2. The dielectric constant of air is $\epsilon(\text{air}) \approx 1$ and that of fused silica $\epsilon(SiO_2) \approx 2.1$ [59] in the visible regime. The real part of the dielectric constant of silicon at $E = 2$ eV is $\epsilon(\text{Si}) \approx 15$ [60]. In our fit we could reproduce approximately the real part of $\epsilon(SiO_2)$. Since the antenna is not embedded in a silica matrix we think that the antenna could feel the dielectrics of the silicon underneath the 400 nm silica layer.

Another aspect is the amplitude of the PL spectrum. In Fig. 4.6 are the experimental spectra of the same monopole ($\lambda_0 = 532$ and 633 nm) compared with the fitted model function. We find for the ($\lambda_0 =$) 633 nm excitation a $4\times$ higher intensity whereas the model predicts a $10\times$ larger amplitude.

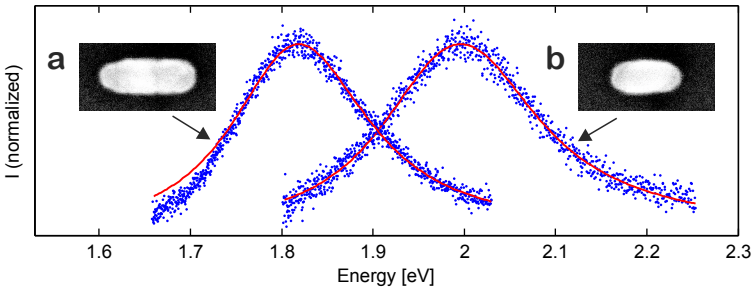

Figure 4.5: Two spectra (λ_0 = 532 nm) with their corresponding fit to the model [51]. In the fit all data points $<$ 1.73 eV and $>$ 2.18 eV were excluded. **(a)** Longer monopole (a_{SEM} = 95 nm, b_{SEM} = 34 nm) fitted to ϵ_m = 2.18 + 0.04i ($\bar{R}^2$ = 0.98) and **(b)** shorter monopole (a_{SEM} = 71 nm, b_{SEM} = 36 nm) fitted to ϵ_m = 2.11 + 0.08i ($\bar{R}^2$ = 0.97).

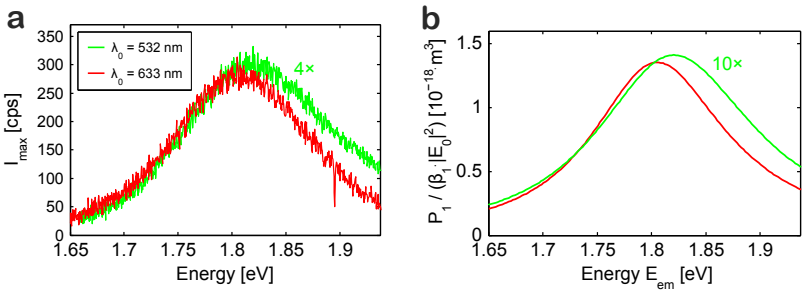

Figure 4.6: **(a)** Spectra of the same antenna (a_{SEM} = 96 nm, b_{SEM} = 37 nm) excited with two lasers and **(b)** their corresponding fits to the model [51]. The fit results are ϵ_m = 2.20 + 0.02i ($\bar{R}^2$ = 0.98) and ϵ_m = 2.25 + 0.03i ($\bar{R}^2$ = 0.97) for λ_0 = 532 nm and 633 nm, respectively. The measurements show a 4$\times$ higher intensity for λ_0 = 633 nm whereas the model predicts a 10$\times$ higher amplitude.

4.2 Interband Absorption Edge

4.2.1 Observation of an Additional Peak

In section 4.1.1 we mentioned the broad and non-Lorentzian spectra of long monopole antennas. Here, we want to discuss their physical background more in detail.

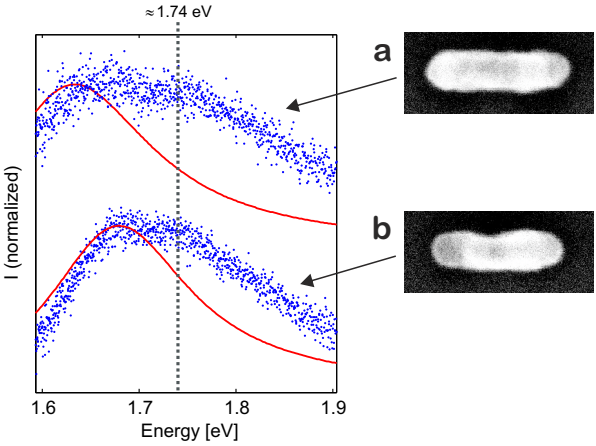

Figure 4.7: Spectra for two different monopole antennas (λ_0 = 532 nm and $P \approx$ 500 µW) with an overlay by the model function [51]. The dielectric constant of the environment is assumed to be ϵ_m = 2.18 + 0.04i. The geometries taken from SEM images are **(a)** a_{SEM} = 119 nm, b_{SEM} = 35 nm and **(b)** a_{SEM} = 108 nm, b_{SEM} = 34 nm. The left shoulder of the peak still follows the model function whereas the right shoulder remains at the energy of approximately 1.74 eV.

Figure 4.7 shows two spectra from different antennas. We calculate the model function with the geometrical dimensions (a_{SEM} and b_{SEM}) from SEM images. The dielectric constant (ϵ_m = 2.18 + 0.04i) is assumed to be the same like in Fig. 4.5a. The model does not fit to the entire spectrum. It only describes the left shoulder of the peak. The right shoulder at higher energy remains at the value of approximately 1.74 eV. We attribute the left shoulder to the plasmonic resonance of the monopole antenna.

4.2.2 Explanations

In Fig. 4.7 the right shoulder of both spectra is located at the energy of approximately 1.74 eV. We argue that the shoulder originates from the onset in the joint density of states. S. Eustis *et al.* [53] argue that in the gold PL spectra this feature is always present and its intensity depends how close the plasmon energy comes to the interband absorption edge. In our measurements we see this feature only if the expected plasmon energy is below the absorption edge. We think that this behavior is not excluded in the work of Eustis *et al.* [53] since they used a distribution of different aspect ratios. Even if the average plasmon resonance lies above the absorption edge, a small part of plasmon energies might be below the edge and can trigger the additional peak.

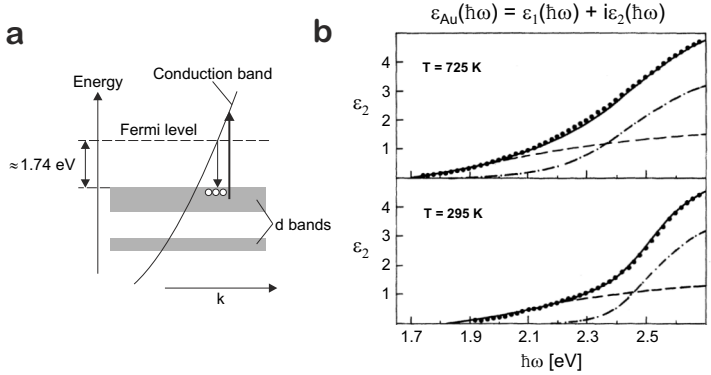

Figure 4.8: (a) Schematics of the electronic band structure of gold near the X symmetry point. The additional peak (1.74 eV) in the PL spectrum corresponds to the onset in the joint density of states of the upper d-band and the sp-conduction band. **(b)** Interband contribution of the dielectric constant ϵ_2 at different temperatures [61]. Dashed line corresponds to the X transitions contribution and dashed dotted line to L transitions contribution. Dotted and solid line are the experimental and theoretical total curve, respectively. At room temperature we expect an onset at ≈ 1.8 eV and at 452 °C an onset at ≈ 1.7 eV.

The interband absorption edge is primarily determined by interband transitions between the upper d-band and the sp-conduction band near the X symmetry point (see Fig. 4.8). Possible transitions near the L symmetry point refer to a higher energy onset (Fig. 4.8b). We expect that under a continuous irradiation the gold nanostructure is heated up above the room temperature. This would explain that

the peak energy in our measurements (1.74 eV) corresponds to the interband absorption edge between 1.7 eV (room temperature) and 1.8 eV (452 °C).

4.2.3 z-Dependence of the Luminescence

We further investigated the behaviour of the interband absorption edge while changing the focus in z-direction. Figure 4.9 shows two examples in which the laser focus was varied in z. The spectra at $z = 0$ corresponds to a maximum photoluminescence of the nanostructure.

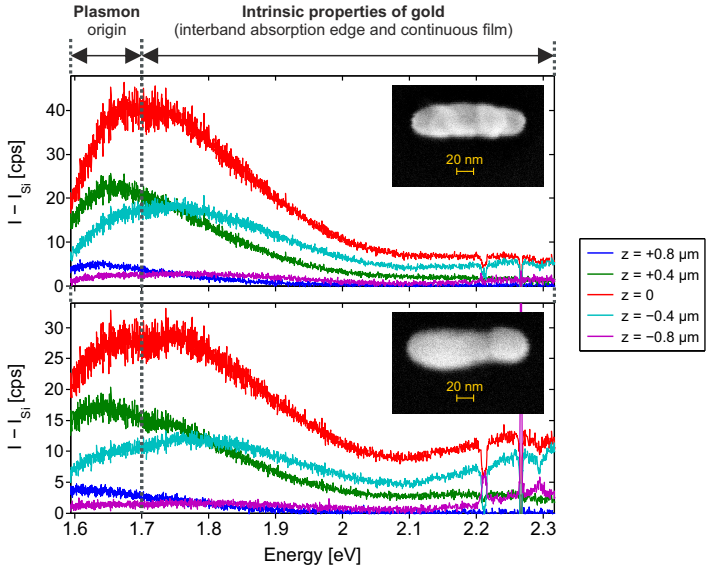

Figure 4.9: Two examples of PL spectra of long monopoles ($\lambda_0 = 532$ nm and $P \approx 2$ mW). The laser focus was varied between $z = +0.8$ µm and $z = -0.8$ µm in which $z = 0$ corresponds to the point of maximum luminescence. At low energy (< 1.7 eV) the plasmonic peak is visible. At higher energy the interband absorption peak (1.7–1.8 eV) and a peak above 2.1 eV are visible. The latter one could correspond to the intrinsic luminescence of a gold film.

We can distinguish between two regimes. At $z > 0$ we observe a pronounced peak (< 1.7 eV) which is originated from the plasmon of the antenna. While moving the laser focus further to the sample ($z < 0$), the plasmonic peak gets

less dominant and the peak (1.7–1.8 eV) of the interband absorption edge is becoming stronger. Interestingly at the same time we observe a stronger peak above 2.1 eV which could correspond to the intrinsic photoluminescence of gold (compare Fig. 3.9). Contrary to the z-coordinate, we do not see any relative peak variations while moving the laser focus within the xy-plane.

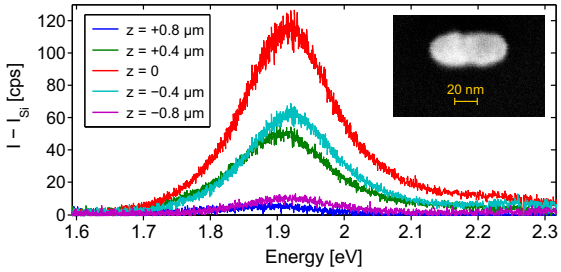

Figure 4.10: Two PL spectra of short monopoles (λ_0 = 532 nm and $P \approx 500$ µW). The laser focus was varied between $z = +0.8$ µm and $z = -0.8$ µm. Beside the plasmonic peak at approximately 1.9 eV there is no peak at the interband absorption edge.

In Fig. 4.10 the spectra of a shorter monopole antenna are presented. The peak according to the plasmon resonance is visible at approximately 1.9 eV. For all z-positions of the laser focus we do not observe any feature at the interband absorption edge (1.7–1.8 eV). This clarifies that we see the latter peak only for a long monopole if its plasmon energy is below the interband absorption edge. The spectrum at $z = 0$ corresponds to maximum photoluminescence.

4.3 Summary

We studied the gold photoluminescence of monopole antennas. The peak energy of the luminescence spectrum is redshifted towards longer nanostructures whereas the peak amplitude reaches a maximum at the length of $a_{SEM} \approx 90$ nm. We applied a model which attributes the luminescence spectrum of the nanostructure to the intrinsic luminescence of gold which is enhanced by the particle plasmon. For longer monopoles we observe an additional peak at approximately 1.74 eV. We argue that this feature is caused by the onset of interband transitions near the X symmetry point of gold.

CHAPTER 5

PHOTOLUMINESCENCE OF GOLD NANOSTRUCTURES – DIPOLES

Two gold nanostructures feel the local electric field of their neighbour when their separation is less than the incident wavelength. In this chapter we focus on the electromagnetic coupling of monopole antennas which are closely located to each other. The emitted photoluminescence (PL) spectrum of gold is our tool of investigation.

5.1 Dependence on Interparticle Separation

5.1.1 Experimental Results

We measured the gold luminescence of dipole antennas with variable gap size. The antennas are lithographically fabricated so that monopole separations of $g_{SEM} \approx 10$ nm are possible. The dimensions of one single arm is constant within the variations of the lithography process. We will discuss two different cases. In the first one (Fig. 5.2) the monopole arms ($a_{SEM} = 65 \pm 2$ nm) are shorter than the length (a_{SEM}) of an isolated monopole whose PL amplitude (I_{max}) is a maximum. In the second case (Fig. 5.3) the monopole arms ($a_{SEM} = 103 \pm 4$ nm) are longer than the length of an isolated monopole with maximal PL amplitude. In Fig. 4.2a as well as Fig. 4.3a the length dependence of I_{max} shows a maximum at $a_{SEM} \approx 90$ nm.

In both cases we observe a significant redshift of the peak position (E_{max}) towards smaller gaps (Figs. 5.2b and 5.3b). When the monopole separation grows, the resonance energy E_{max}(dipole) converges to the energy of an isolated monopole E_{max}(monopole) with the corresponding length.

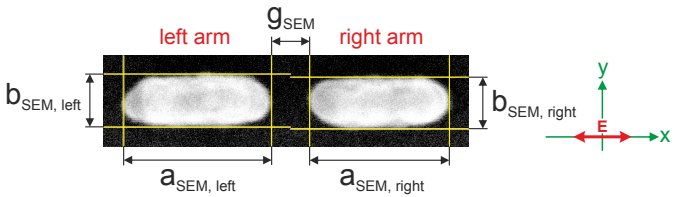

Figure 5.1: Geometry of the dipole antenna is taken from a SEM image. The average values of the antenna length and width is defined as $a_{SEM} = (a_{SEM,left} + a_{SEM,right})/2$ and $b_{SEM} = (b_{SEM,left} + b_{SEM,right})/2$, respectively.

The peak amplitude (I_{max}) behaves differently in both cases. If two monopoles are coupled and their length is smaller than the resonance length ($a_{SEM} \approx 90$ nm) of an isolated monopole, we see an increase in I_{max} towards shorter gaps. We explain this trend by the shift of the peak energy E_{max}. The closer the monopoles come the smaller is E_{max}. For isolated monopoles a smaller E_{max} corresponds to an increased length (a_{SEM}) which results in a more intense PL spectrum. Therefore, a dipole antenna with shrinking gap size behaves like an isolated monopole being elongated. And the elongation of the monopole would enlarge the light absorption and emission what appears in an increased amplitude I_{max} (see Fig. 4.2a).

We can also apply this explanation to the second case. Here, the monopoles are longer ($a_{SEM} = 103 \pm 4$ nm) than the expected resonance length in Fig. 4.3a. When the distance between two monopoles is reduced, then they would behave like an isolated monopole which is becoming longer. This elongated monopole absorbs and emits less light. Hence, we measure a lower PL spectrum (or I_{max}) for dipole antennas with smaller gap sizes.

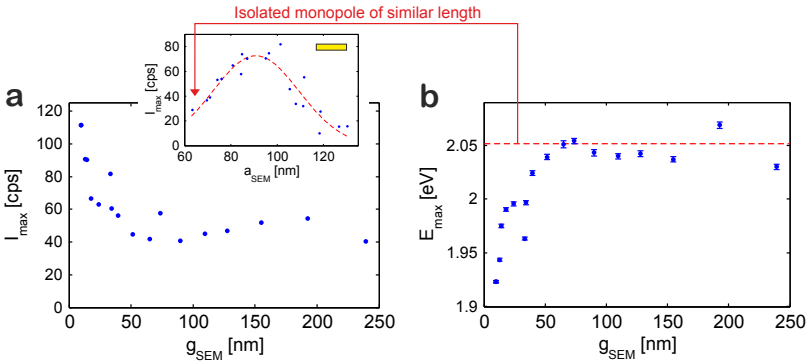

Figure 5.2: Gap dependence of dipole antennas (a_{SEM} = 65 ± 2 nm, b_{SEM} = 35 ± 2 nm). The laser wavelength and power were λ_0 = 532 nm and $P \approx 500\,\mu W$, respectively. **(a)** Intensity of the gold luminescence vs. gap size. The intensity increases rapidly for smaller gaps. The inset marks a monopole of a similar length with an arrow and the dashed line (Gaussian fit) is a guide to the eye. **(b)** Position of the PL peak. In the gap interval where the intensity increases we observed a redshift for E_{max} towards smaller gaps . The red dashed line shows the energy position of a monopole with similar length.

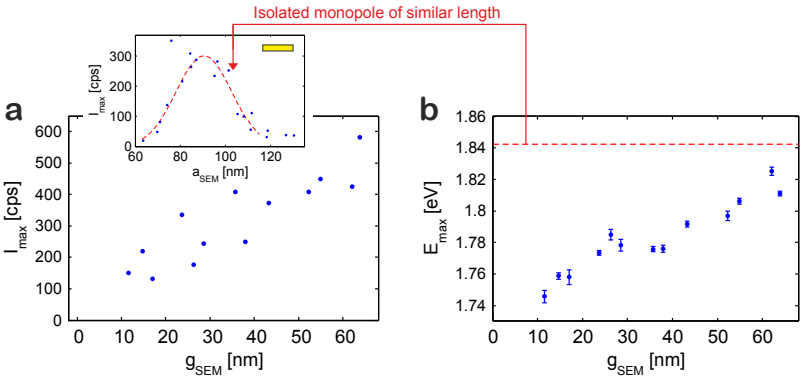

Figure 5.3: Gap dependence of dipole antennas (a_{SEM} = 103 ± 4 nm, b_{SEM} = 36 ± 2 nm). The laser wavelength and power were λ_0 = 633 nm and $P \approx 200\,\mu W$, respectively. **(a)** Intensity of the gold luminescence vs. gap size. The intensity decreases towards smaller gaps. The inset marks a monopole of a similar length with an arrow and the dashed line (Gaussian fit) is a guide to the eye. **(b)** Position of the PL peak. We observed a redshift for E_{max} towards smaller gaps. The red dashed line shows the energy position of a monopole with similar length.

5.1.2 Plasmon Hybridization

K.-H. Su *et al.* [62] and W. Rechberger *et al.* [63] were observing a redshift in the scattering and extinction spectra of gold nanoparticles with decreasing gap size. This redshift can be described by the fractional shift $\triangle\lambda/\lambda$ in the plasmon resonance wavelength [64–66]. λ is the resonance wavelength of an isolated monopole and $\triangle\lambda = \lambda_{Dipole} - \lambda_{Monopole}$ represents the difference between resonance wavelengths of isolated and coupled monopoles.

$$\left(\frac{\triangle\lambda}{\lambda}\right) = A \cdot \exp\left(\frac{-S/D}{\tau}\right) \tag{5.1}$$

An empiric function to describe the fractional shift is given in Eq. 5.1. In this formula A is a prefactor and τ an exponential coupling decay length. S is the interparticle edge-to-edge separation and D the particle dimension along the axis of interaction. In our measurements S and D would correspond to g_{SEM} and a_{SEM}, respectively.

$$\left(\frac{\triangle\lambda}{\lambda}\right) = \frac{1}{12\Lambda(S/D+2)^3 - (\gamma+1)} \tag{5.2}$$

Another formula (Eq. 5.2) is analytically derived from the near-field coupling of two nanoparticles [64]. The nanoparticle shape are approximated by oblate spheroids where the interparticle interaction is in the plane of the circular cross-sections of the spheroids. S is approximately the interparticle separation (g_{SEM}) and D is the particle dimension (a_{SEM}). Λ and γ are shape dependent variables which are introduced as follows. The electric dipole moment $\overrightarrow{\mu}$ of a particle in an electric field $\overrightarrow{E}$ is:

$$\overrightarrow{\mu} = \epsilon_m \overleftrightarrow{\alpha} \overrightarrow{E}$$

in the quasi-static limit where $\overleftrightarrow{\alpha}$ is the dipole polarizability tensor. In the case of a spheroidal particle the dipole polarizability α_n along the principal axis n (= 1,2,3) is described by the Clausius-Mossotti formula [67, 68]:

$$\alpha_n = \epsilon_0(1+\gamma)\left(\frac{\epsilon-\epsilon_m}{\epsilon+\gamma\epsilon_m}\right)V \tag{5.3}$$

ϵ_0 is the vacuum permittivity and V the particle volume which is introduced as:

$$V = \frac{1}{6}\pi D^3 \Lambda \tag{5.4}$$

The shape factor Λ is defined as the reciprocal aspect ratio ($\Lambda = b/a = 1/R_{SEM}$) of the oblate spheroid where a (= D) is the dimension in the plane of interaction.

The parameter γ in Eq. 5.3 is directly related to the depolarization factor A_n and the lightning-rod factor L_{LR} of the corresponding axis:

$$\gamma = A_n^{-1} - 1 = L_{LR} - 1 \tag{5.5}$$

For the spherical limit ($a = b$) the depolarization factor takes the value $A = \frac{1}{3}$ and therefore γ is 2.

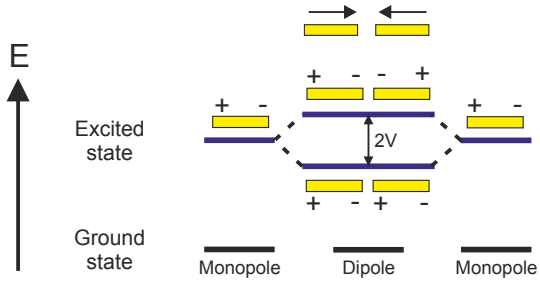

Figure 5.4: Schematics of the plasmonic hybridization due to near-field coupling of two identical monopoles. The excited energy levels separate by the value $2V$. The higher energy state is forbidden since the two dipole moments are summed to zero.

The redshift of the plasmon resonance can also be described by a hybridization of excited energy levels (Fig. 5.4). Originally an energy splitting was discussed for two coupled excitons [69]. Within the molecular exciton coupling theory (MECT) the Simpson-Peterson approximation [70] describes the energy difference V of two identical levelled excitons:

$$V_{Exciton} = \frac{|\mu^2|}{n_m^2 \cdot R^3} \cdot |\kappa| \tag{5.6}$$

where μ is the transition dipole moment of the system, n_m the refractive index of the medium and R the center-to-center separation of the dipole moments. The orientation factor κ is:

$$\kappa = (\cos\theta_{12} - 3\cos\theta_{1R}\cos\theta_{2R})$$

where θ_{12} is the angle between the two dipole vectors, θ_{1R} and θ_{2R} the angles between the dipole vectors and the interparticle axis.

C. Tabor *et al.* [66] applied this exciton model to the coupling of two nanoparticles having the identical plasmon energy:

$$V_{Plasmon} \approx n_m^2 \cdot |\mu^2| \cdot |\kappa| \cdot \Gamma \tag{5.7}$$

Here, n_m is the refractive index of the surrounding medium, μ the transition dipole module and κ an orientation factor:

$$\kappa = (\cos\theta_{1P} + \cos\theta_{2P})(\cos\theta_{12} - 3\cos\theta_{1R}\cos\theta_{2R})$$

where θ is the angle between axes which are expressed in the indices. The indices 1 and 2 stand for the axes of the induced dipole moments, R represents the interparticle axis and P the polarization axis of the light. Γ is a function which characterize the fractional plasmon shift $\triangle\lambda/\lambda$ and can take on either the exponential (Eq. 5.1) or the analytically derived formula (Eq. 5.2).

5.1.3 Plasmon Ruler Equation

The plasmon ruler Eq. 5.2 was originally derived to describe the fractional shift $\triangle\lambda/\lambda$ in scattering or extinction spectra. We use this formula for our gold PL spectra since they are similarly dominated by the particle plasmons (see chapter 4). The fitting results of the experimental data (see Figs. 5.2 and 5.3) are shown in Fig. 5.5.

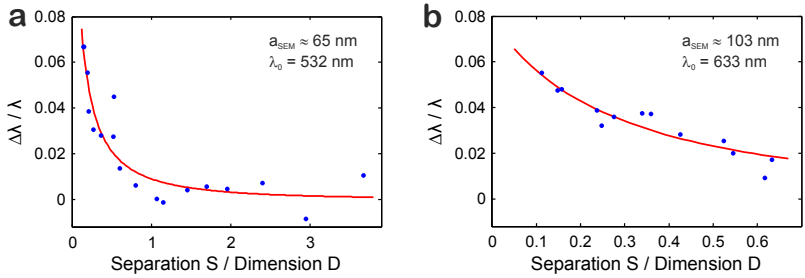

Figure 5.5: The trend of E_{max} is described by the plasmon ruler Eq. 5.2. **(a)** Experimental data of Fig. 5.2 is fitted to the shape factors $\Lambda = 0.46 \pm 0.25$ and $\gamma = 39 \pm 31$ ($\bar{R}^2 = 0.86$). **(b)** Data of Fig. 5.3 is fitted to the shape factors $\Lambda = 0.33 \pm 0.11$ and $\gamma = 18 \pm 14$ ($\bar{R}^2 = 0.87$).

We assign the separation S and the particle dimension D to the gap size g_{SEM} and the antenna length a_{SEM}, respectively. The shape dependent variables Λ and γ are the fit parameters to be determined.

The first case (Fig. 5.5a) leads to the results $\Lambda = 0.46 \pm 0.25$ and $\gamma = 39 \pm 31$. From SEM images we measure the geometry to be $a_{SEM} = 65 \pm 2$ nm and $b_{SEM} = 35 \pm 2$ nm what gives an aspect ratio of $R_{SEM} = 1.9 \pm 0.1$. This would correspond to a $\Lambda_{SEM} = 0.54 \pm 0.03$ according to Eq. 5.4. The lightning-rod factor

is L_{LR} = 5.5 at R_{SEM} = 1.9 for a prolate spheroid approximation of a monopole (see section 4.1.2). This would result in γ_{SEM} = 4.5 according to Eq. 5.5. The calculated value Λ_{SEM} (= 0.54) agrees well with the fit results Λ = 0.46 $\pm$ 0.25 whereas γ_{SEM} (= 4.5) differs from the fit result γ = 39 $\pm$ 31. One reason of this deviation could be the rather coarse shape approximation of the monopole antennas by oblate spheroids. The second reason could lie in the variation of the fabrication process. If the geometry of the two coupled monopoles is not identical within the nanometer range, the resulting PL spectrum will be an overlap of two non-superimposable spectra.

The fit results of the second case (Fig. 5.5b) are Λ = 0.33 $\pm$ 0.11 and γ = 18 $\pm$ 14. The monopole dimension taken from SEM images is a_{SEM} = 103 $\pm$ 4 nm and b_{SEM} = 36 $\pm$ 2 nm leading to an aspect ratio of R_{SEM} = 2.9 $\pm$ 0.2. The calculated parameters would be Λ_{SEM} = 0.35 $\pm$ 0.02 and γ_{SEM} = 7.8 regarding Eqs. 5.4 and 5.5, respectively. These values agree well with the parameters Λ and γ determined in the fit.

5.2 Summary

We measured the gold photoluminescence of two near-field coupled monopole antennas. The gap between the antennas are varied whereas the dimension of the monopoles itself is kept constant within the variation of the lithography process. We see a redshift in the plasmon resonance (E_{max}) towards smaller gap sizes which we fitted by a plasmon ruler equation. The amplitude of the luminescence (I_{max}) is either decreasing ($a_{SEM} > \approx$ 90 nm) or increasing ($a_{SEM} < \approx$ 90 nm) while reducing the particle separation.

Chapter 6

Conclusion and Outlook

We studied two differently terminated benzodifuran molecules in a mechanically controllable break junction. The molecules were either capped by pyridyl (BDF_{NN}) or acetylthiol (BDF_{SS}) groups and can therefore attach to gold electrodes creating an electrical contact. The backbone of these molecules is derived from oligo(phenylene ethynylene) which is an established conductive wire in the field of molecular electronics. The central benzodifuran unit is optically active and can interact with the electronic orbitals via photon absorption.

The opening traces of BDF_{SS} show long conductance plateaus in the order of 0.75–2 nm electrode separation, whereas to BDF_{NN} belongs only very short plateaus of 0.075–0.2 nm.

The statistical distribution of the conductance plateaus delivers more insight. We found two main conductance intervals. For BDF_{SS} the upper interval ($\log_{10}(\langle G\rangle/G_0)$ = -3.9...-2.7) contains 2–3$\times$ more plateaus than the lower interval ($\log_{10}(\langle G\rangle/G_0)$ = -5.7...-4.7). Both intervals indicate that the thiol ends as well as the cyanide groups can bind to gold. The higher conductance interval would correspond to a Au-S-BDF_{SS}-S-Au bridging and its average conductance value is fitted to be $3.6 \cdot 10^{-4}\, G_0$.

Nanoscale antennas were fabricated by electron beam lithography with the aim of plasmonic applications. We investigated the plasmonic properties via their gold photoluminescence. The gold antennas were excited by two different laser wavelengths (532 and 633 nm) and the emission of the antennas were collected in a broad wavelength range of approximately 550–860 nm.

At first we tested the photoluminescence (PL) under the perspective of power dependence, spatial and temporal stability, incident light polarization and enhancement compared to that of an unstructured film. The fluorescence signal shows a high orientation of the electric field parallel to the long antenna axis. Therefore we aligned the polarization always along this axis. One crucial issue is the incident laser power focused onto the nanostructure. A too high intensity

can damage the gold nanostructure irreversibly, which is immediately observable in the spectrum. A lower laser power decreases the signal-to-noise ratio which makes the analysis more difficult. We found a compromise between structural stability and signal-to-noise ratio. The detected photoluminescence is proportional to the incident power. This verifies the single-photon absorption in this PL process.

The gold photoluminescence of monopole antennas follows well a model which explains the enhancement of the intrinsic luminescence by presence of a localized plasmon. The peak energy of the PL spectrum is redshifted for longer nanostructures whereas the peak amplitude reaches a maximum at the monopole length of $a_{SEM} \approx 90\,\text{nm}$. Interestingly for long antennas the spectra deviate from the model and show an additional peak. The latter peak shows no geometrical dependence and remains at the energy value of the interband absorption edge (1.7–1.8 eV) of gold. By varying the z-position of the laser focus one can see variations in the amplitudes of both peaks.

As the next step we studied the photoluminescence of dipole antennas where the individual monopole antennas are coupled by their near-field. The PL spectra of dipole antennas show a redshift of E_{max} towards smaller gap sizes. We relate this behaviour to the increased coupling of individual arms via their optical near-field. This redshift can be qualitatively described by a plasmon ruler equation. The amplitude of the luminescence (I_{max}) is either decreasing ($a_{SEM} >\approx 90\,\text{nm}$) or increasing ($a_{SEM} <\approx 90\,\text{nm}$) while reducing the particle separation.

In our work we studied the electrical properties of two optically active molecules and the plasmonic properties of nanoantennas separately. Both parts can be merged together to a full characterization of optically active molecules. The properties of antennas were studied with the help of the gold photoluminescence since it is closely related to the plasmonic properties. The emission of the gold is a step before the study of emitting fluorescent molecules.

In the future we want to electrically contact separated gold nanostructures. This would allow a combination of nanoelectronics with plasmonic behaviour of the gold antennas. One promising candidate as the contacting material is graphene. A few layer graphene can electrically bridge the gap between the main circuit line and the isolated nanoantenna without significantly perturbing the plasmonic characteristics of the antenna. An additional approach is to use dipole antennas with a gap comparable to the length of a molecule. This gap size similar to that of a break junction would make electrical measurements possible while still using the plasmonic properties of the antenna.

Bibliography

[1] A. Aviram and M. A. Ratner, *Molecular rectifiers*, Chemical Physics Letters **29**, 277 (1974).

[2] C. Joachim, J. K. Gimzewski, and A. Aviram, *Electronics using hybrid-molecular and mono-molecular devices*, Nature **408**, 541 (2000).

[3] N. J. Tao, *Electron transport in molecular junctions*, Nature Nanotechnology **1**, 173 (2006).

[4] G. Binnig, H. Rohrer, C. Gerber, and E. Weibel, *Surface studies by scanning tunneling microscopy*, Physical Review Letters **49**, 57 (1982).

[5] B. Xu and N. J. Tao, *Measurement of single-molecule resistance by repeated formation of molecular junctions*, Science **301**, 1221 (2003).

[6] Z. M. Wu, M. Steinacher, R. Huber, M. Calame, S. J. van der Molen, and C. Schönenberger, *Feedback controlled electromigration in four-terminal nanojunctions*, Applied Physics Letters **91**, 053118 (2007).

[7] J. S. Agustsson, *Arrays of Gold Nanoparticles as a Platform for Molecular Electronics*, Ph.D. thesis, University of Basel (2012).

[8] S. J. van der Molen, J. Liao, T. Kudernac, J. S. Agustsson, L. Bernard, M. Calame, B. J. van Wees, B. L. Feringa, and C. Schönenberger, *Light-controlled conductance switching of ordered metal-molecule-metal devices*, Nano Letters **9**, 76 (2009).

[9] S. Link and M. A. El-Sayed, *Shape and size dependence of radiative, non-radiative and photothermal properties of gold nanocrystals*, International Reviews in Physical Chemistry **19**, 409 (2000).

[10] M. Pelton, J. Aizpurua, and G. Bryant, *Metal-nanoparticle plasmonics*, Laser & Photonics Reviews **2**, 136 (2008).

[11] H. A. Atwater and A. Polman, *Plasmonics for improved photovoltaic devices*, Nature Materials **9**, 205 (2010).

[12] P. Zijlstra, P. M. R. Paulo, and M. Orrit, *Optical detection of single non-absorbing molecules using the surface plasmon resonance of a gold nanorod*, Nature Nanotechnology **7**, 379 (2012).

[13] N. Yu, P. Genevet, M. A. Kats, F. Aieta, J.-P. Tetienne, F. Capasso, and Z. Gaburro, *Light propagation with phase discontinuities: Generalized laws of reflection and refraction*, Science **334**, 333 (2011).

[14] S. Kim, J. Jin, Y.-J. Kim, I.-Y. Park, Y. Kim, and S.-W. Kim, *High-harmonic generation by resonant plasmon field enhancement*, Nature **453**, 757 (2008).

[15] D. M. O'Carroll, C. E. Hofmann, and H. A. Atwater, *Conjugated polymer/metal nanowire heterostructure plasmonic antennas*, Advanced Materials **22**, 1223 (2010).

[16] K. Kneipp, Y. Wang, H. Kneipp, L. Perelman, I. Itzkan, R. Dasari, and M. Feld, *Single molecule detection using surface-enhanced Raman scattering (SERS)*, Physical Review Letters **78**, 1667 (1997).

[17] S. Nie and S. R. Emory, *Probing single molecules and single nanoparticles by surface-enhanced Raman scattering*, Science **275**, 1102 (1997).

[18] D. R. Ward, F. Hüser, F. Pauly, J. C. Cuevas, and D. Natelson, *Optical rectification and field enhancement in a plasmonic nanogap*, Nature Nanotechnology **5**, 732 (2010).

[19] D. R. Ward, N. J. Halas, J. W. Ciszek, J. M. Tour, Y. Wu, P. Nordlander, and D. Natelson, *Simultaneous measurements of electronic conduction and Raman response in molecular junctions*, Nano Letters **8**, 919 (2008).

[20] D. R. Ward, N. K. Grady, C. S. Levin, N. J. Halas, Y. Wu, P. Nordlander, and D. Natelson, *Electromigrated nanoscale gaps for surface-enhanced Raman spectroscopy*, Nano Letters **7**, 1396 (2007).

[21] K. J. Savage, M. M. Hawkeye, R. Esteban, A. G. Borisov, J. Aizpurua, and J. J. Baumberg, *Revealing the quantum regime in tunnelling plasmonics*, Nature **491**, 574 (2012).

[22] C. Péterfalvi, I. Grace, and C. Lambert, *Electron transport in benzo-difuran molecular wires*, Poster at the Mid-term Review Meeting (FUNMOLS) in Malvern (England) (2010).

[23] C. Yi, C. Blum, M. Lehmann, S. Keller, S.-X. Liu, G. Frei, A. Neels, J. Hauser, S. Schürch, and S. Decurtins, *Versatile strategy to access fully functionalized benzodifurans: Redox-active chromophores for the construction of extended π-conjugated materials*, Journal of Organic Chemistry **75**, 3350 (2010).

[24] H. Li, C. Schubert, P. O. Dral, R. D. Costa, A. La Rosa, J. Thüring, S.-X. Liu, C. Yi, S. Filippone, N. Martín, S. Decurtins, T. Clark, and D. M. Guldi, *Probing charge transfer in benzodifuran-C_{60} dumbbell-type electron donor-acceptor conjugates: Ground- and excited-state assays*, Journal of Chemical Physics and Physical Chemistry **14**, 2910 (2013).

[25] H. Li, C. Yi, S. Moussi, S.-X. Liu, C. Daul, M. Grätzel, and S. Decurtins, *Benzo[1,2-b:4,5-b']difuran-based sensitizers for dye-sensitized solar cells*, RSC Advances **3**, 19798 (2013).

[26] H. Li, P. Jiang, C. Yi, C. Li, S.-X. Liu, S. Tan, B. Zhao, J. Braun, W. Meier, T. Wandlowski, and S. Decurtins, *Benzodifuran-based π-conjugated copolymers for bulk heterojunction solar cells*, Macromolecules **43**, 8058 (2010).

[27] J. G. Brunner, *Gaining Microscopic Insight into Molecular Junctions by Transport Experiments*, Ph.D. thesis, University of Basel (2012).

[28] L. Grüter, M. T. González, R. Huber, M. Calame, and C. Schönenberger, *Electrical conductance of atomic contacts in liquid environments*, Small **1**, 1067 (2005).

[29] S. Wu, *Electrical Conductance of Single Conjugated Oligomers*, Ph.D. thesis, University of Basel (2009).

[30] Z. Li, H. Li, S. Chen, T. Fröhlich, C. Yi, C. Schönenberger, M. Calame, S. Decurtins, S.-X. Liu, and E. Borguet, *Regulating a benzodifuran single molecule redox switch via electrochemical gating and optimization of molecule/electrode coupling*, Journal of the American Chemical Society **136**, 8867 (2014).

[31] S. Grunder, R. Huber, V. Horhoiu, M. T. González, C. Schönenberger, M. Calame, and M. Mayor, *New cruciform structures: Toward coordination induced single molecule switches*, Journal of Organic Chemistry **72**, 8337 (2007).

[32] S. Grunder, R. Huber, S. Wu, C. Schönenberger, M. Calame, and M. Mayor, *Oligoaryl cruciform structures as model compounds for coordination-induced single-molecule switches*, European Journal of Organic Chemistry **5**, 833 (2010).

[33] R. Huber, M. T. González, S. Wu, M. Langer, S. Grunder, V. Horhoiu, M. Mayor, M. R. Bryce, C. Wang, R. Jitchati, C. Schönenberger, and M. Calame, *Electrical conductance of conjugated oligomers at the single molecule level*, Journal of the American Chemical Society **130**, 1080 (2008).

[34] X. Jiao, J. Goeckeritz, S. Blair, and M. Oldham, *Localization of near-field resonances in bowtie antennae: Influence of adhesion layers*, Plasmonics **4**, 37 (2009).

[35] O. L. Muskens, V. Giannini, J. A. Sánchez-Gil, and J. Gómez Rivas, *Optical scattering resonances of single and coupled dimer plasmonic nanoantennas*, Optics Express **15**, 17736 (2007).

[36] R. M. Bakker, V. P. Drachev, Z. Liu, H.-K. Yuan, R. H. Pedersen, A. Boltasseva, J. Chen, J. Irudayaraj, A. V. Kildishev, and V. M. Shalaev, *Nanoantenna array-induced fluorescence enhancement and reduced lifetimes*, New Journal of Physics **10**, 125022 (2008).

[37] G. Zoriniants and W. L. Barnes, *Fluorescence enhancement through modified dye molecule absorption associated with the localized surface plasmon resonances of metallic dimers*, New Journal of Physics **10**, 105002 (2008).

[38] *Datasheet - 19923 Fluorescent Red 633*, Fluka.

[39] L. Gunnarsson, T. Rindzevicius, J. Prikulis, B. Kasemo, M. Käll, S. Zou, and G. C. Schatz, *Confined plasmons in nanofabricated single silver particle pairs: Experimental observations of strong interparticle interactions*, Journal of Physical Chemistry B **109**, 1079 (2005).

[40] A. Mooradian, *Photoluminescence of metals*, Physical Review Letters **22**, 185 (1969).

[41] N. E. Christensen and B. O. Seraphin, *Relativistic band calculation and the optical properties of gold*, Physical Review B **4**, 3321 (1971).

[42] T. Dieing, O. Hollricher, and J. Toporski, *Confocal Raman Microscopy* (Springer, 2011).

[43] A. Kuhlicke, S. Schietinger, C. Matyssek, K. Busch, and O. Benson, *In situ observation of plasmon tuning in a single gold nanoparticle during controlled melting*, Nano Letters **13**, 2041 (2013).

[44] S.-S. Chang, C.-W. Shih, C.-D. Chen, W.-C. Lai, and C. R. C. Wang, *The shape transition of gold nanorods*, Langmuir **15**, 701 (1999).

[45] L. Novotny, *Effective wavelength scaling for optical antennas*, Physical Review Letters **98**, 266802 (2007).

[46] J. Gersten and A. Nitzan, *Electromagnetic theory of enhanced Raman scattering by molecules adsorbed on rough surfaces*, Journal of Chemical Physics **73**, 3023 (1980).

[47] G. T. Boyd, T. Rasing, J. R. R. Leite, and Y. R. Shen, *Local-field enhancement on rough surfaces of metals, semimetals, and semiconductors with the use of optical second-harmonic generation*, Physical Review B **30**, 519 (1984).

[48] C. K. Chen, T. F. Heinz, D. Ricard, and Y. R. Shen, *Surface-enhanced second-harmonic generation and Raman scattering*, Physical Review B **27**, 1965 (1983).

[49] E. Dulkeith, T. Niedereichholz, T. A. Klar, J. Feldmann, G. von Plessen, D. I. Gittins, K. S. Mayya, and F. Caruso, *Plasmon emission in photoexcited gold nanoparticles*, Physical Review B **70**, 205424 (2004).

[50] C. Sönnichsen, T. Franzl, T. Wilk, G. von Plessen, and J. Feldmann, *Drastic reduction of plasmon damping in gold nanorods*, Physical Review Letters **88**, 077402 (2002).

[51] G. T. Boyd, Z. H. Yu, and Y. R. Shen, *Photoinduced luminescence from the noble metals and its enhancement on roughened surfaces*, Physical Review B **33**, 7923 (1986).

[52] M. B. Mohamed, V. Volkov, S. Link, and M. A. El-Sayed, *The 'lightning' gold nanorods: Fluorescence enhancement of over a million compared to the gold metal*, Chemical Physics Letters **317**, 517 (2000).

[53] S. Eustis and M. A. El-Sayed, *Aspect ratio dependence of the enhanced fluorescence intensity of gold nanorods: Experimental and simulation study*, Journal of Physical Chemistry B **109**, 16350 (2005).

[54] P. B. Johnson and R. W. Christy, *Optical constants of the noble metals*, Physical Review B **6**, 4370 (1972).

[55] D.-S. Wang, F.-Y. Hsu, and C.-W. Lin, *Surface plasmon effects on two photon luminescence of gold nanorods*, Optics Express **17**, 11350 (2009).

[56] K. Imura, T. Nagahara, and H. Okamoto, *Near-field two-photon-induced photoluminescence from single gold nanorods and imaging of plasmon modes*, Journal of Physical Chemistry B **109**, 13214 (2005).

[57] P. Biagioni, M. Celebrano, M. Savoini, G. Grancini, D. Brida, S. Mátéfi-Tempfli, M. Mátéfi-Tempfli, L. Duò, B. Hecht, G. Cerullo, and M. Finazzi, *Dependence of the two-photon photoluminescence yield of gold nanostructures on the laser pulse duration*, Physical Review B **80**, 045411 (2009).

[58] P. Biagioni, D. Brida, J.-S. Huang, J. Kern, L. Duò, B. Hecht, M. Finazzi, and G. Cerullo, *Dynamics of four-photon photoluminescence in gold nanoantennas*, Nano Letters **12**, 2941 (2012).

[59] I. H. Maltison, *Interspecimen comparison of the refractive index of fused silica*, Journal of the Optical Society of America **55**, 1205 (1965).

[60] M. A. Green, *Self-consistent optical parameters of intrinsic silicon at 300 K including temperature coefficients*, Solar Energy Materials and Solar Cells **92**, 1305 (2008).

[61] P. Winsemius, M. Guerrisi, and R. Rosei, *Splitting of the interband absorption edge in Au: Temperature dependence*, Physical Review B **12**, 4570 (1975).

[62] K.-H. Su, Q.-H. Wei, X. Zhang, J. J. Mock, D. R. Smith, and S. Schultz, *Interparticle coupling effects on plasmon resonances of nanogold particles*, Nano Letters **3**, 1087 (2003).

[63] W. Rechberger, A. Hohenau, A. Leitner, J. R. Krenn, B. Lamprecht, and F. R. Aussenegg, *Optical properties of two interacting gold nanoparticles*, Optics Communications **220**, 137 (2003).

[64] P. K. Jain, W. Huang, and M. A. El-Sayed, *On the universal scaling behavior of the distance decay of plasmon coupling in metal nanoparticle pairs: A plasmon ruler equation*, Nano Letters **7**, 2080 (2007).

[65] P. K. Jain and M. A. El-Sayed, *Universal scaling of plasmon coupling in metal nanostructures: Extension from particle pairs to nanoshells*, Nano Letters **7**, 2854 (2007).

[66] C. Tabor, D. Van Haute, and M. A. El-Sayed, *Effect of orientation on plasmonic coupling between gold nanorods*, ACS Nano **3**, 3670 (2009).

[67] H. Morgan and N. G. Green, *AC Electrokinetics: Colloids and Nanoparticles* (Research Studies Press, 2003) pp. 33–47.

[68] U. Kreibig and M. Vollmer, *Optical Properties of Metal Clusters* (Springer, 1995).

[69] M. Kasha, H. R. Rawls, and M. A. EL-Bayoumi, *The exciton model in molecular spectroscopy*, Pure and Applied Chemsitry **11**, 371 (1965).

[70] B. Z. Packard, D. D. Toptygin, A. Komoriya, and L. Brand, *Intramolecular resonance dipole-dipole interactions in a profluorescent protease substrate*, Journal of Physical Chemistry B **102**, 752 (1998).

[71] M. Castro-Lopez, D. Brinks, R. Sapienza, and N. F. van Hulst, *Aluminum for nonlinear plasmonics: Resonance-driven polarized luminescence of Al, Ag, and Au nanoantennas*, Nano Letters **11**, 4674 (2011).

[72] D. Groom, *Cosmic rays and other nonsense in astronomical CCD imagers, in Scientific detectors for astronomy* (Springer, 2004) pp. 81–94.

Appendix A

Fabrication Methods

A.1 Break Junctions

General overview of steps:

1. Cleaning the steel substrate
2. Spin coating of polyimide on the substrate
3. Spin coating of PMMA resist
4. Electron beam lithography (EBL) and resist development
5. Metallization and lift-off
6. Polyimide film and UV lithography
7. Reactive ion etching before the measurement

Cleaning the substrate

1. Substrate (spring steel 65 mm $\times$ 65 mm, thickness = 0.3 mm)
2. Cleaned with acetone soaked tissue
3. Sonication in acetone (30 min)
4. UV ozone for 10 min (Model 42-220, Jelight Company)
5. Sonication in 2-propanol (30 min)
6. Dried with N_2

Spin Coating of Polyimide on Steel Substrate

1. Spin coating of polyimide (3×)
2. Substrate baked on hotplate
3. Vacuum annealing at ≈350 °C for 1 h
4. Laser cutting to dimensions of 24 mm × 10 mm

Spin Coating of the PMMA Resist

1. Cleaning of the substrate
   Sonication in acetone, rinsed in 2-propanol
2. Spin coated ≈110 nm PMMA/MA 33 % (AR-P 617.03, Allresist) (4000 rpm, 40 s, ramp 4 s) and annealed on hotplate (10 min, 200 °C)
3. Spin coated 400–500 nm PMMA 950k (AR-P 671.09, Allresist) diluted with chlorobenzene (4000 rpm, 40 s, ramp 4 s) and annealed on hotplate (10 min, 180 °C)
4. Applied gold colloids (diameter of 50 and 200 nm) for EBL focusing

Electron beam lithography

- Zeiss Supra 35 lithography system (high voltage = 10 kV)
- Write field size (Aperture) =
  3750 and 1000 µm (120 µm) and 100 µm (10 µm)
- Area Step Size (Aperture) = 200 nm (120 µm) and 20 nm (10 µm)
- Area dose = 150 µC/cm^2
- Line dose = 1000 pC/cm
- Structure developed in (1:3 v/v) 4-methyl-2-pentanone/2-propanol (45 s) and rinsed in 2-propanol

Metallization

- Balzers-Pfeiffer PLS 500
- Deposition rate = 1 Å/s
- Sample temperature $< 0\,^{\circ}\mathrm{C}$

1. 10 nm Ti in a tilted angle of 47° normal to the surface
2. 60 nm Au
3. Lift-off in $\approx 50\,^{\circ}\mathrm{C}$ warm acetone with the help of a syringe

Polyimide film and UV lithography

1. Photosensitive polyimide (HD-4104, HD MicroSystems) spin coated (4000 rpm, ramp 4 s, 60 s)
2. Annealed on hotplate at 85 °C (2 min) followed by 95 °C (2 min)
3. Lithography at the UV mask aligner (MJB4, Süss MircoTec, Germany)
   - contact ends and 10 µm stripe on junction covered by a mask
   - intensity = 33 mW/s^2
   - exposure time = 6.5 s
4. Post-baked at 80 °C (60 s)
5. Developed (50 s) and rinsed (15 s)
6. Vacuum annealing at $\approx$350–370 °C for 1 h

Reactive Ion Etching

- Oxford Instruments Plasmalab$^{80\ \mathrm{Plus}}$
- Base pressure = $5 \cdot 10^{-5}$ mbar
- Process pressure = 100 mTorr
- Gas flow: 32 % O_2, 1.5 % CHF_3 and 66.5 % N_2
- RF Power = 400 W
- Plasma duration = 2 min 40 s

A.2 Nanoscale Antennas

General overview of steps:

1. Cleaning the substrate
2. Spin coating of PMMA resist
3. Electron beam lithography and resist development
4. Metallization and lift-off
5. Ar ion sputtering before the measurement

Cleaning the substrate

1. Silicon wafer (low doped, thermally oxidized with $\approx 400\,\text{nm}$ SiO_2) cut into pieces of $\approx 10\,\text{mm} \times 8\,\text{mm}$
2. Sonication in acetone (5 min)
3. Rinsed in 2-propanol and dried

Spin Coating of the PMMA Resist

1. Spin coated $\approx 110\,\text{nm}$ PMMA-MA (4000 rpm, 40 s, ramp 4 s) and annealed on hotplate (10 min, 200 °C)
2. Spin coated $\approx 90\,\text{nm}$ PMMA (4000 rpm, 40 s, ramp 4 s) and annealed on hotplate (10 min, 180 °C)
3. Applied gold colloids (diameter of 50 and 200 nm) for EBL focusing

Electron beam lithography

- Zeiss Supra 40 lithography system (high voltage = 30 kV)
- Working distance = 8.7 mm
- Write field size (Aperture) = 1000 µm (120 µm) and 100 µm (7.5 µm)
- Area Step Size (Aperture) = 100 nm (120 µm) and 10 nm (7.5 µm)
- Line Step Size (Aperture) = 5 nm (7.5 µm)
- Area dose = 240 $\mu C/cm^2$

- Line dose = 1000 pC/cm
- Structure developed in (1:3 v/v) 4-methyl-2-pentanone:2-propanol (90 s) and rinsed in 2-propanol

Metallization

- Sharon thermal evaporator
- Sample temperature $\approx -90\,^{\circ}\mathrm{C}$

1. 0.5 nm Ti (deposition rate = 0.4 Å/s)
2. 50 nm Au (deposition rate = 1 Å/s)
   direct or 2×25 nm in tilted angles of $\pm 2.5°$ normal to the surface
3. lift-off in $\approx 50\,^{\circ}\mathrm{C}$ warm acetone with the help of a syringe

Argon Ion Sputtering

- Oxford Instruments Plasmalab$^{80\ \mathrm{Plus}}$
- Pressure = $5 \cdot 10^{-5}$ mbar stabilized with Ar flow
- Power = 20 mA
- Extraction voltage = 0.6 kV
- Ion energy = 1 kV
- Sputter time = 4 min 19 s
  (corresponds to 5 nm Au with a rate of 1.2 nm/min)

Optical Dark-Field Photographies

- Optical microscope Olympus MX51 in dark-field mode
  no additional light filters used
- Objective Olympus MPLFLN-BD 100x, numerical aperture (NA) = 0.9
- Digital camera Canon 350D with settings:
  auto white balance (AWB) and ISO 400

Creating the EBL Structure by a Script

The design of the antenna structures were generated by a separate script. This ensures a good control over the geometry of up to 40'000 antennas on one sample. The design is saved as an .asc file and can easily be imported into the software Elphy 5.0 (Raith). The principle of writing the antenna structure is shown in Fig. A.1a. The electron beam traces a rectangular loop twice in order to receive maximum smoothness on the edges. The vertical separation of the lines (b_{Design}) is 10 nm which leads to an antenna width of b_{SEM} = 30–40 nm.

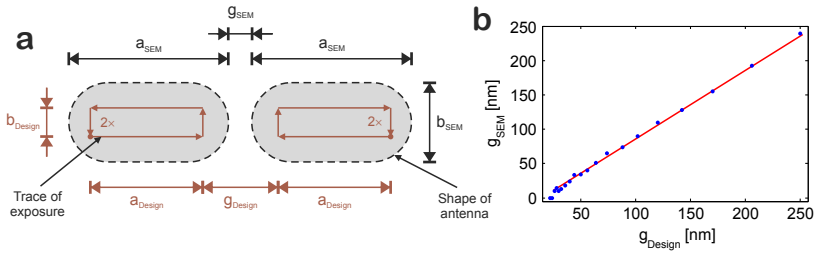

Figure A.1: (a) Schematics of electron-beam lithography of a dipole antenna and the dimensions. Each antenna is written twice by a closed trace in order to smooth the edges. The length (a_{SEM}), width (b_{SEM}) and gap (g_{SEM}) are the nanostructure dimensions in the SEM image and a_{Design}, b_{Design} and g_{Design} are the corresponding dimensions in the design. **(b)** Relation between design (g_{Design}) and final antenna gap (g_{SEM}). The red line correspond to the linear fit $g_{SEM} = g_{Design} - 14$ nm.

An excerpt from the C script which creates an importable EBL structure for Raith Elphy 5.0:

```
#include <stdio.h>
#include <stdlib.h>
#include <math.h>

/* .asc file for import in Elphy 5.0 */
FILE *asc;

/* creates a line path for the EBL structure of one single antenna arm   */
/* (start_U,start_V) = start point of the line path [um]                 */
/* d_lines = line separation [um]                                        */
/* size = length of antenna arm [um]                                     */
/* dose = dose factor in Elphy 5.0 [%]                                   */
/* layer = layer number in EBL structure                                 */
void box_by_lines(double start_U, double start_V, double d_lines,
                  double size, double dose, int layer)
```

```
{
int i;

/* writes point of the line path in file */
#define in_asc(U_,V_) (fprintf(asc,"%.3f %.3f\n",U_,V_))

fprintf(asc,"L %.1f %d %.3f\n",dose*50,layer,0);
in_asc(start_U     ,start_V);
in_asc(start_U+size,start_V);
in_asc(start_U+size,start_V+d_lines);
in_asc(start_U     ,start_V+d_lines);
in_asc(start_U     ,start_V);
in_asc(start_U+size,start_V);
in_asc(start_U+size,start_V+d_lines);
in_asc(start_U     ,start_V+d_lines);
in_asc(start_U     ,start_V);
fprintf(asc,"#\n");
}

/* creates the EBL structure of a monopole antenna                    */
/* (c_U,c_V) = center point of antenna [um]                           */
/* arm = arm length [um]                                              */
/* dose = dose factor in Elphy 5.0 [%]                                */
/* layer = layer number in EBL structure                              */
void antenna_by_lines
  (double c_U, double c_V, double arm, double dose, int layer)
{
box_by_lines(c_U-floor(arm*500)/1000,c_V-0.005,0.01,arm,dose,layer);
}

/* creates the EBL structure of a dipole antenna                      */
/* (c_U,c_V) = center point of antenna [um]                           */
/* arm = arm length [um]                                              */
/* gap = gap size [um]                                                */
/* dose = dose factor in Elphy 5.0 [%]                                */
/* layer = layer number in EBL structure                              */
void dipole_antenna_by_lines
  (double c_U, double c_V, double arm, double gap, double dose, int layer)
{
box_by_lines(c_U-gap/2-arm,c_V-0.005,0.01,arm,dose,layer);
box_by_lines(c_U+gap/2+arm,c_V-0.005,0.01,-arm,dose,layer);
}

/* creates the EBL structure of an asymmetric dipole antenna          */
/* (c_U,c_V) = center point of antenna [um]                           */
/* l_arm = left arm length [um]                                       */
/* r_arm = right arm length [um]                                      */
/* gap = gap size [um]                                                */
/* dose = dose factor in Elphy 5.0 [%]                                */
/* layer = layer number in EBL structure                              */
void asym_dipole_antenna_by_lines
  (double c_U, double c_V, double l_arm, double r_arm, double gap,
   double dose, int layer)
{
box_by_lines(c_U-gap/2-l_arm,c_V-0.005,0.01,l_arm,dose,layer);
box_by_lines(c_U+gap/2+r_arm,c_V-0.005,0.01,-r_arm,dose,layer);
}
```

```
/* creates the EBL structure of a vertically arranged dipole antenna     */
/* (c_U,c_V) = center point of antenna [um]                              */
/* arm = arm length [um]                                                 */
/* gap = vertical gap size [um]                                          */
/* dose = dose factor in Elphy 5.0 [%]                                   */
/* layer = layer number in EBL structure                                 */
void vert_dipole_antenna_by_lines
  (double c_U, double c_V, double arm, double gap, double dose, int layer)
{
box_by_lines(c_U-floor(arm*500)/1000,c_V-floor(gap*500)/1000-0.01,0.01,arm,
             dose,layer);
box_by_lines(c_U-floor(arm*500)/1000,c_V+ceil(gap*500)/1000,0.01,arm,
             dose,layer);
}
```

Appendix B

Measurements – Setup and Parameters

B.1 Break Junctions – Molecular Measurements

Components of the Break Junction Setup

- Stepper motor Phythron GLD electronically controlled by a computer
  1 motor step corresponds to a vertical push rod movement of $\triangle z$ = 25 nm and is divided into 8 substeps
- IV converter SP895c/d (University of Basel)
  Autoranging from 10^{-4} to 10^{-9} V/A and connected to a switching spike killer
- Series resistor of 1 kΩ limits the maximum current, bias voltage = 0.2 V
- Electrical connections between clamps of the apparatus and the gold circuits of the sample by soft indium pads
- National Instruments (NI) data acquisition board (DAQ)
- Liquid cell (PEEK, glass) contains ≈ 1 ml of solution and is pressed by a flexible Viton o-ring onto the sample

B.2 Nanoscale Antennas – Photoluminescence

Components of the Raman Microscope

- Confocal Raman microscope WITec alpha300 on optical table (vibration isolated)
- Frequency-doubled Nd:YAG laser ($\lambda_0 \approx 532$ nm), P = 50 mW

- HeNe laser ($\lambda_0 \approx 633\,\text{nm}$), P = 35 mW
- Spectrometer UHTS 300 with
  multi-mode fiber (pinhole size = 50 µm) connected to microscope
- Half-wave plates for changing light polarization
- Reflectance grating 600 grooves/mm, see appendix C.3
  blaze wavelength $\approx 500\,\text{nm}$, spectral range $> 130\,\text{nm}$
- CCD sensor Andor DV401-BV-352, see appendix C.2
  cooled down to −60 °C, peak quantum efficiency $\approx 550\,\text{nm}$
  1024 × 127 pixels with pixel size 26 × 26 [µm]
  ReadMode in Full Vertical Binning (FVB), read-out time = 12.21 ms
  Vertical Shift Speed = 8.25 µs
  Horizontal Shift Speed = 0.1 MHz
  Preamplifier Gain = 1
- Objective Olympus MPLFLN 100x, numerical aperture (NA) = 0.9,
  working distance (WD) = 1 mm, field number (FN) = 26.5 mm
- Piezoelectric scan stage, travel range = 200 (x) × 200 (y) × 20 (z) [µm]
- Optical power meter Thorlabs PM100D
- ArHg spectral calibration lamp

B.2.1 General Steps in the Measurement

Calibration of the microscope before measurements:

1. Adjust microscope by maximizing Si Raman peak ($520\,\text{cm}^{-1}$)
   Light coupling into the glass fiber to the spectrometer was optimized by using x-/y-screws.
2. Align sample on the scan stage
   The fabricated structures on sample were aligned with the coordinate system of the scan stage. The long axis of antennas corresponds to the x-axis of the stage.
3. Align polarization of the laser
   The laser polarization was optimized by maximizing the photoluminescence signal of a gold monopole antenna.

Measurement procedure of a nanostructure:

1. Locate one gold nanostructure by a fast two-dimensional scan
   An xy-scan was performed around the expected position of a nanostructure. The total scan size was 3 µm × 3 µm (pixel separation = 100 nm) and the integration time per pixel 62 ms.

2. Maximize signal by changing the laser focus in x, y and z
   The scan stage position relative to the laser focus was optimized for the maximum photoluminescence.

3. Make sure if the signal is stable in time
   In a time series of recorded spectra (duration = 32 s) the stability of the luminescence signal was proven.

4. Take a spectrum of the nanostructure
   The photoluminescence spectrum was recorded at the optimized position of the laser focus. The integration time was 212 ms and 100–200 accumulations were performed.

5. Take a background spectrum
   Either a silicon spectrum in 1–2 µm distance (xy-plane) from the nanostructure or a spectrum without laser excitation was used as the background (see appendix C.1). The integration time was 212 ms and 100–200 accumulations were performed.

B.2.2 Experimental Errors

In the photoluminescence measurements we identified different sources of experimental errors. The emission intensity of the photoluminescence (I_{max}) can vary less than ± 10 % within a measurement series of the same day. The error of measurements on different days can be estimated to be $< \pm 17$ %.

We consider following error sources (I_{max}):

Incident light polarization A mismatch of the polarization along the antenna axis can cause a reduced intensity. We estimate this error by less than ± 2 %.

Defocus and focal stability The laser was focused manually onto a nanostructure and the luminescence spectrum can therefore differ from the optimum. By focusing on the same nanostructure at different times we estimate this error by $< \pm 6$ %.

Microscope alignment With the x-/y-screws one defines how well the light is coupled into the multi-mode fiber to the spectrometer. We determined the maximum intensity (P = 1 mW) of the silicon Raman peak (520 cm^{-1}) at the beginning of each measurement day in order to evaluate the alignment. We can estimate a deviation of less than ± 7 % between different days.

Laser power fluctuations The laser power can fluctuate by $< \pm 2$ % within a single measurement.

Appendix C

Photoluminescence – Spectral Normalization and Combination

In this chapter we discuss the analytical treatment of the measured spectra. The microscope is recording each spectrum in the units [CCD counts]. Since we also detect the dark current (I_0) of the CCD chip, we need to subtract it as a background from the spectrum. The result (Eq. C.1) is finally normalized by the quantum efficiency of the CCD sensor, the percentaged vignetting, the integration time and the incident laser power. This normalized spectrum (I_{norm}) is expressed in units [cps] and makes it easier to compare spectra of different measurements.

$$I_{norm}\left(p_{CCD}\right)\,[\text{cps}] = \frac{\left(I\left(p_{CCD}\right) - I_{background}\left(p_{CCD}\right)\right)\ [\text{CCD counts}]}{f_{CCD}\left(E(p_{CCD})\right) \cdot f_V\left(p_{CCD}\right) \cdot t\ [\text{s}] \cdot P\ [\text{mW}]} \tag{C.1}$$

C.1 Spectral Background

We define either the dark current of the CCD chip (I_0) or the silicon spectrum close to a nanostructure (I_{Si}) as the background $I_{background}$. The background spectrum is subtracted from each photoluminescence spectrum. I_0 was measured without any laser excitation at the microscope and is not time-dependent (Fig. C.1b). In case of gold nanostructures we used the silicon spectrum (I_{Si}) nearby (in 1–2 µm distance) for the background (see Fig. C.1a).

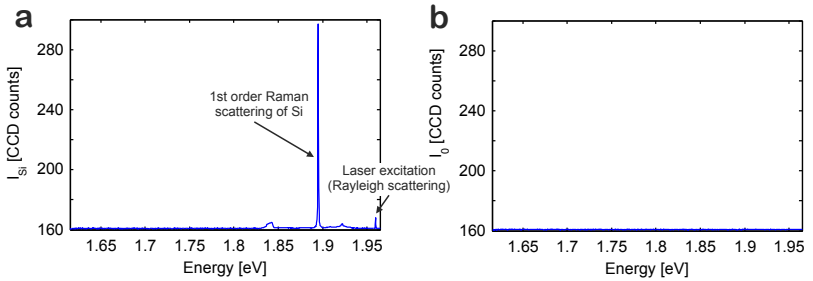

Figure C.1: (a) Silicon spectrum (I_{Si}) at λ_0 = 633 nm and $P \approx 1$ mW. **(b)** Measured spectrum (I_0) without any excitation by a laser.

C.2 Quantum Efficiency of the CCD Sensor

In the normalization we used the relative quantum efficiency (QE) of the CCD sensor chip (Andor DV401A-BV-352). The quantum efficiency provided by the Andor company is in Fig. C.2 given for the temperatures −50 °C and −70 °C. In our experiments we cooled down the sensor chip to −60 °C. Therefore we calculated the average of the two temperatures quoted in Fig. C.2.

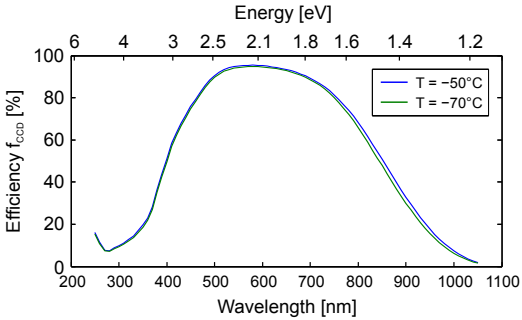

Figure C.2: Relative quantum efficiency (QE) of the Andor CCD sensor DV401A-BV-352 at −50 °C and −70 °C. The QE(λ) values at −60 °C used for normalization are calculated by the average of the values at −50 °C and −70 °C.

C.3 Reflectance Efficiency of the Spectrometer Grating

In our measurements we used a 600 grooves/mm grating. Its reflectance efficiency is wavelength dependent with the maximum at ≈ 500 nm (blaze wavelength). The reflectance efficiency is not included in the spectral normalization.

The reflectance efficiency of a master grating is presented in Fig. C.3. Depending on the incident light polarization (s- or p-polarized) the efficiency is changing. In the experiments of this work the polarization of the emitted light is not detected. M. Castro-Lopez *et al.* [71] studied the polarization of two-photon photoluminescence of gold nanoantennas. The emitted light was found to be nearly unpolarized.

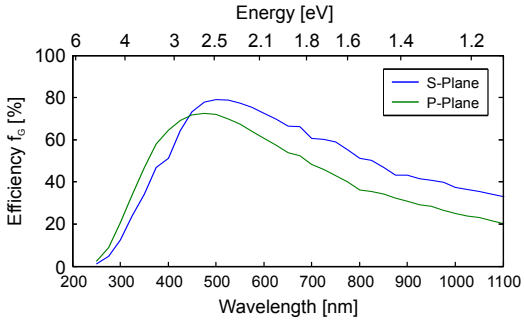

Figure C.3: Absolute reflectance efficiency of a 600 grooves/mm master grating (blaze wavelength = 500 nm) depending on the polarization of the incident light (S and P). The data was delivered by Newport Inc. (USA).

C.4 Optical Vignetting of the Raman Spectrometer

Vignetting is in the photography a well known effect where the light intensity falls off close to the edges of the image. Here, inside the Raman spectrometer we observe a similar effect. The intensity of a Raman peak is dependent on the position on which it is detected at the CCD sensor. At the edges of the CCD chip we receive significantly less intensity (or [CCD counts]).

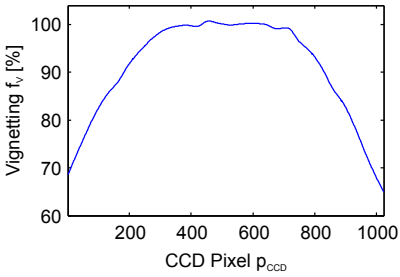

Figure C.4: Optical vignetting inside the spectrometer dependent on the CCD pixel number. The calibration curve was measured by using the Stokes peak of silicon (520 cm^{-1}) at λ_0 = 532 nm.

In Fig. C.4 the relative intensity is presented dependent on the CCD pixel p_{CCD}. It was determined using the Raman peak of silicon ($\approx$ 520 cm^{-1}) at λ_0 = 532 nm. By definition for the pixel p_{CCD} = 513 the optical vignetting is set to 1. This pixel corresponds to the current center wavelength λ_c of the grating. The vignetting effect is approximately independent from the center wavelength.

C.5 Spectra Combination

After the normalization according to Eq. C.1, spectra of different wavelength ranges can be combined. This allows us to receive a spectrum with a much wider range than that which is possible with the 600 grooves/mm grating (≈ 130–140 nm). An example of combination is shown in Fig. C.5. It is composed by 3 individual spectra (at the same laser focus position x, y and z) whose center wavelengths λ_c are shifted by 60 nm.

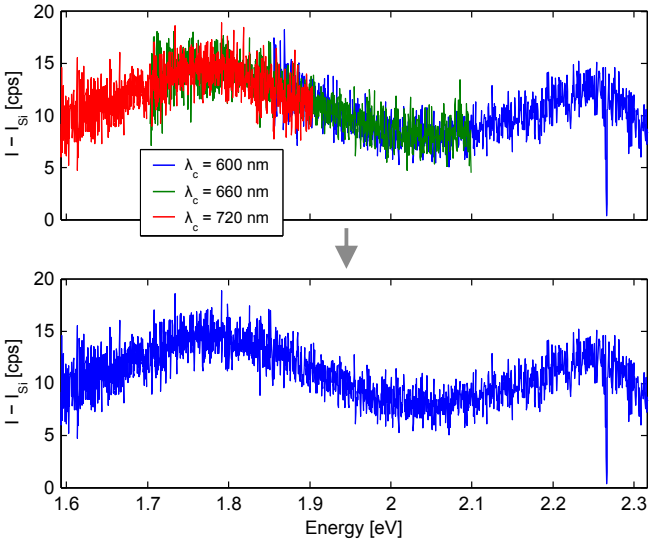

Figure C.5: Spectrum which is composed by 3 spectra measured at different center wavelengths λ_c. The measurements was done at λ_0 = 532 nm (2.33 eV) and $P \approx 1$ mW with the spectrometer grating 600 grooves/mm.

C.6 Cosmic Ray Removal

It can happen that we detect very sharp peaks in the photoluminescence spectra like it is shown in Fig. C.6. Their origin is by cosmic ray generated charged muons hitting the CCD sensor and therefore give an additional signal which does not belong to the photoluminescence measurement [72]. We filter out these peaks by an algorithm described in [42] and which is implemented in the WITec Project software.

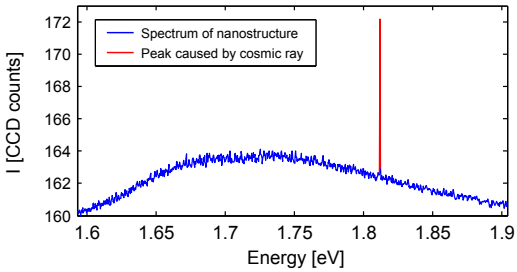

Figure C.6: Measured spectrum of a gold nanostructure (blue) which contains a very sharp peak (red) caused by cosmic ray. This sharp peak can be detected and eliminated by an algorithm.

Appendix D

Data Analysis

D.1 Break Junctions – Molecular Measurements

D.1.1 Cycle dependent Diagrams

All diagrams were created by Matlab scripts directly from the raw data of the break junction measurements.

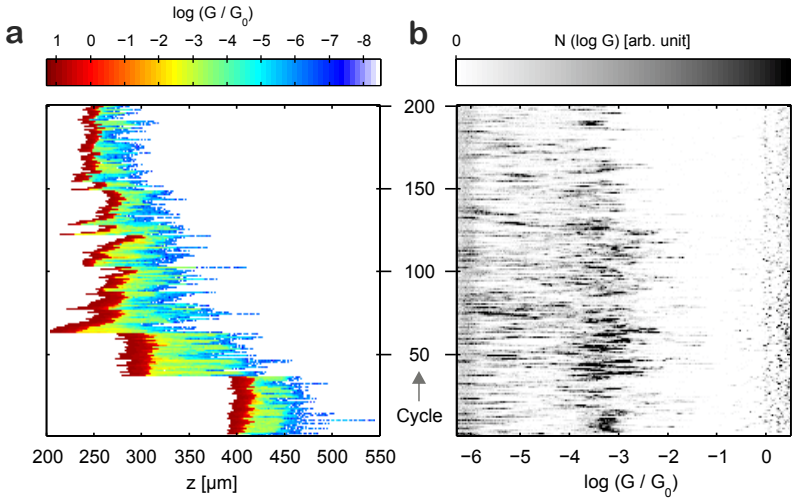

Figure D.1: Diagrams of 200 consecutive opening traces. **(a)** Dependence of the conductance value $\log(G/G_0)$ on the push rod position z and **(b)** histogram of logarithmic conductance values.

In Fig. D.1 two different diagrams are shown dependent on the cycle number. Figure D.1a visualizes the conductance values for each push rod position z and cycle number. Here, it is possible to diagnose the quality of the gold break junction. Sudden changes in the z-onset of the trace can illustrate worsening of the junction.

Figure D.1b shows conductance histograms in each cycle. The logarithmic conductance axis $\log(G/G_0)$ is divided into intervals of width $\triangle \log(G/G_0) = 0.03$. In this diagram one can track molecular conductance peaks in time.

D.1.2 Logarithmic Conductance Histograms

Another possibility is to use all traces of a whole series in one single histogram. In Fig. D.2a the logarithmic conductance values $\log(G/G_0)$ vs. their corresponding push rod position z is summed up in a two-dimensional histogram. Here, the conductance traces are pinned at the conductance of $G_{ref} = 0.5\,G_0$. The intervals in the z- and $\log(G/G_0)$-axis are 0.5 µm and 0.05 wide, respectively. The background level at approximately $10^{-6}\,G_0$ is dependent on the junction, the noise level of the environment and the solvent.

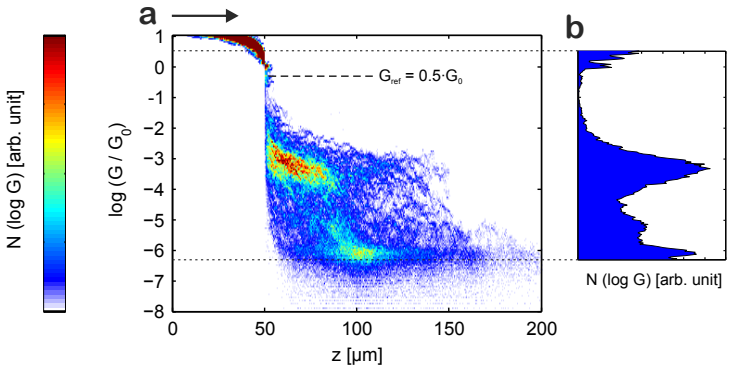

Figure D.2: Logarithmic histograms of conductance values. **(a)** The two-dimensional histogram counts the frequency of $\log(G/G_0)(z)$ data points of individual traces. Here, all traces are pinned a $G_{ref} = 0.5\,G_0$. **(b)** One-dimensional histogram without z-dependence.

In the one-dimensional histogram (Fig. D.2b) the frequency of the conductance values are counted in 0.03 wide intervals. Figure D.2b can be understood as a projection of the two-dimensional histogram (Fig. D.2a) onto the conductance axis.

D.2 Nanoscale Antennas – Photoluminescence

D.2.1 Estimating the Geometry in SEM Images

In order to estimate the geometry of the antenna nanostructures we used high-resolution SEM images. The working distance was kept to 3–4 mm at an extraction voltage of 20 kV in order to receive a sufficient contrast by the InLense detector.

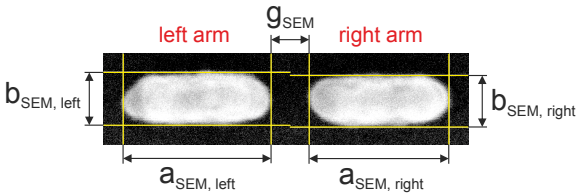

Figure D.3: High resolution SEM image of a dipole antenna. The geometry is determined by a box around each dipole arm. Here, the left arm has the dimension $a_{SEM,left}$ = 108 nm × $b_{SEM,left}$ = 38 nm and the right arm $a_{SEM,right}$ = 102 nm × $b_{SEM,right}$ = 38 nm. The edge-to-edge separation between both arms is g_{SEM} = 28 nm.

In Fig. D.3 is the principle illustrated. The dimensions are determined by drawing a box around a single gold nanostructure. Length (*a*), width (*b*) and gap (*g*) are the side lengths and the box separation, respectively. The box drawing is automatically done by a Matlab script:

```
nNA=20; % total number of antennas
f00_SEM_length=zeros(1,nNA); % average length of both arms
f00_SEM_length_err=zeros(1,nNA); % length difference between both arms
f00_SEM_gap=zeros(1,nNA); % gap size
f00_SEM_width=zeros(1,nNA); % average width of both arms
f00_SEM_width_err=zeros(1,nNA); % width difference between both arms

px2nm=0.4466; % ratio 1 [pixel] in SEM image / 1 [nm]
thresh=0.002; % gray threshold for boundaries
EBLmin=45; % mimumum size [pixel] of one arm

for j=1:nNA % loop for each antenna
  length1=false;
  length2=false;
  length1_b=0;
  length2_b=0;
  temp=shiftdim(f00_SEM2(j,:,:)); % get SEM image in gray scale
  temp=sum(temp,1)/max(sum(temp,1)); % normalize SEM image

  % evaluate both lengths and gap size
  for i=1:size(temp,2)
```

```
    if (temp(i)>=thresh)
      if (length1_b==0)
        length1=true;
        length1_b=i;
      elseif ((length2_b==0) && ~length1)
        length2=true;
        length2_b=i;
      end
    end
    if ((temp(i)<thresh) && length1)
      length1=false;
      length1_e=i;
      if (length1_e-length1_b<EBLmin)
        length1_b=0;
      end
    end
    if ((temp(i)<thresh) && length2)
      length2=false;
      length2_e=i;
      if (length2_e-length2_b<EBLmin)
        length2_b=0;
      end
    end
  end

  % evaluate width of left arm
  width1=false;
  width1_b=0;
  temp=shiftdim(f00_SEM2(j,:,1:floor((length1_e+length2_b)/2)));
  temp=sum(temp,2)/max(sum(temp,2));
  for i=1:size(temp,1)
    if ((temp(i)>=thresh) && (width1_b==0))
      width1=true;
      width1_b=i;
    end
    if ((temp(i)<thresh) && width1)
      width1=false;
      width1_e=i;
      if (width1_e-width1_b<EBLmin)
        width1_b=0;
      end
    end
  end

  % evaluate width of right arm
  width2=false;
  width2_b=0;
  temp=shiftdim(f00_SEM2(j,:,ceil((length1_e+length2_b)/2):end));
  temp=sum(temp,2)/max(sum(temp,2));
  for i=1:size(temp,1)
    if ((temp(i)>=thresh) && (width2_b==0))
      width2=true;
      width2_b=i;
    end
    if ((temp(i)<thresh) && width2)
      width2=false;
      width2_e=i;
```

```
      if (width2_e-width2_b<EBLmin)
        width2_b=0;
      end
    end
  end

  % calculating final dimensions [nm]
  f00_SEM_length(j)=px2nm*((length1_e-length1_b)+(length2_e-length2_b))/2;
  f00_SEM_length_err(j)=px2nm*((length1_e-length1_b)-...
                          (length2_e-length2_b))/2;
  f00_SEM_gap(j)=px2nm*(length2_b-length1_e);
  f00_SEM_width(j)=px2nm*((width1_e-width1_b)+(width2_e-width2_b))/2;
  f00_SEM_width_err(j)=px2nm*((width1_e-width1_b)-(width2_e-width2_b))/2;
end
```

D.2.2 Lorentzian Fitting of Photoluminescence Spectra

We fitted the measured photoluminescence spectra by a Lorentzian peak function in which the two sides of the peak can have different widths. One example is given in Fig. D.4.

$$y = a \cdot \frac{(\frac{1}{2}c)^2}{(x-b)^2 + (\frac{1}{2}c)^2 \cdot (1 + \mathrm{sign}(x-b) \cdot d)^2} \tag{D.1}$$

The asymmetric Lorentzian curve (Eq. D.1) gives a very good fit to the spectral data and makes it possible to extract key parameters like peak amplitude (I_{max}), peak position (E_{max}) and full width at half maximum (E_{FWHM}).

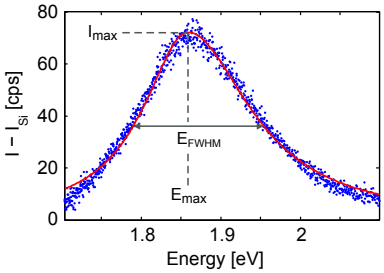

Figure D.4: Photoluminescence spectrum of a gold nanostructure. The spectrum is fitted by an asymmetric Lorentzian peak function in order to extract the amplitude I_{max} (= 70.3 cps), the peak position E_{max} (= 1.86 eV) and the FWHM of the peak E_{FWHM} (= 0.16 eV).

The fitting is performed in two steps by a Matlab script. At first, the entire peak is fitted which gives a good approximation of E_{FWHM}. In the second step a narrower

interval (0.15 eV) around the peak is fitted in order to extract the final peak position and amplitude. In Eq. D.1 and the following Matlab script *a* corresponds to I_{max}, *b* to E_{max}, *c* to E_{FWHM} and *d* is an asymmetry factor of the peak:

```
nSS=16; % total number of spectra
f70_SS_fit1=zeros(nSS,4); % 1st fit parameters a, b, c and d
f70_SS_fit1_err=zeros(nSS,4); % errors of 1st fit parameters a, b, c and d
f70_SS_fit2=zeros(nSS,5); % 2nd fit parameters a, b, c, d and e
f70_SS_fit2_err=zeros(nSS,5); % errors of 2nd fit parameters a, b, c, d, e
f70_SS_fit2_ampl=zeros(1,nSS); % peak amplitudes I_max from 2nd fit

int_Si=[2.2584,2.2729]; % excluded interval [eV] of Si Raman peak
int_g0=[1.593,2.316]; % possible range [eV] for green laser (= 532 nm)
int2=0.15; % narrow interval width [eV] for 2nd fit

fmodel1 = ... % 1st fit model
  fittype('a*c^2*(1+sign(x-b)*d)^2/((x-b)^2+c^2*(1+sign(x-b)*d)^2)',...
                'dependent',{'y'},'independent',{'x'},...
                'coefficients',{'a', 'b', 'c', 'd'});

fmodel2 = ... % 2nd fit model
  fittype('a*c^2*(1+sign(x-b)*d)^2/((x-b)^2+c^2*(1+sign(x-b)*d)^2)+e',...
                'dependent',{'y'},'independent',{'x'},...
                'coefficients',{'a', 'b', 'c', 'd', 'e'});

for i = 1:nSS % loop for each spectrum
  x=f70_eV(:,i); % x values [eV]
  y=f70_SS(:,i); % y values [cps]
  int_b0=[x(1024),x(1)]; % start interval for 1st fit

  % estimate maximum inside allowed starting interval
  int_index=((x>=int_g0(1)) & (x<=int_g0(2))) & ...
            ((x>=int_b0(1)) & (x<=int_b0(2))) & ...
           ~((x>=int_Si(1)) & (x<=int_Si(2)));

  % options for the 1st fit
  options1=fitoptions('method','NonlinearLeastSquares');
  options1.Exclude=excludedata(x,y,'indices',~int_index);
  options.Robust='On';
  options1.TolFun=1e-8;
  options1.TolX=1e-8;
  options1.Lower=[-Inf,-Inf,0,-1];
  options1.Upper=[Inf,Inf,Inf,1];
  options1.Startpoint=[max(y(int_index)),(int_b0(1)+int_b0(2))/2,...
                                         (int_b0(2)-int_b0(1))/2,0];
  fresult = fit(x,y,fmodel1,options1);

  % save fit parameters and their errors (1st fit)
  f70_SS_fit1(i,:)=coeffvalues(fresult);
  temp=confint(fresult);
  f70_SS_fit1_err(i,:)=temp(2,:)-coeffvalues(fresult);
  f70_SS_fit1(i,3)=2*f70_SS_fit1(i,3);
  f70_SS_fit1_err(i,3)=2*f70_SS_fit1_err(i,3);

  % narrow fit interval for 2nd fit (around previous maximum)
  int_b=[f70_SS_fit1(i,2)-int2,f70_SS_fit1(i,2)+int2];
```

```
  int_index=int_index & ((x>=int_b(1)) & (x<=int_b(2)));

  % options for the 2nd fit
  options2=fitoptions('method','NonlinearLeastSquares');
  options2.Exclude=excludedata(x,y,'indices',~int_index);
  options.Robust='On';
  options2.TolFun=1e-8;
  options2.TolX=1e-8;
  options2.Lower=[-Inf,-Inf,0,-1,-1e4];
  options2.Upper=[Inf,Inf,Inf,1,1e4];
  options2.Startpoint(1:4)=f70_SS_fit1(i,:);
  options2.Startpoint(5)=0;
  fresult = fit(x,y,fmodel2,options2);

  % save fit parameters and their errors (2nd fit)
  f70_SS_fit2(i,:)=coeffvalues(fresult);
  temp=confint(fresult);
  f70_SS_fit2_err(i,:)=temp(2,:)-coeffvalues(fresult);
  f70_SS_fit2(i,3)=2*f70_SS_fit2(i,3);
  f70_SS_fit2_err(i,3)=2*f70_SS_fit2_err(i,3);

  % calculate peak amplitude (2nd fit)
  f70_SS_fit2_ampl(i)=f70_SS_fit2(i,1)+f70_SS_fit2(i,5);
end
```

Publications

Journal Publications

- *Regulating a Benzodifuran Single Molecule Redox Switch via Electrochemical Gating and Optimization of Molecule/Electrode Coupling*,
  Z. Li, H. Li, S. Chen, T. Fröhlich, C. Yi, C. Schönenberger, M. Calame, S. Decurtins, S.-X. Liu, and E. Borguet.
  Journal of the American Chemical Society **136**, 8867 (2014).

- *Gold Photoluminescence of Nanoscale Antennas below and above the Interband Absorption Edge*,
  T. Fröhlich, C. Schönenberger, and M. Calame.
  in preparation

Oral Presentations

- *Towards an Optoelectronic Characterization of Molecules*,
  T. Fröhlich, C. Schönenberger, and M. Calame.
  Thematic Workshop (FUNMOLS) in Muggendorf (Germany), April 15-18, 2010.

- *Electrical and Optical Characterization of Fluorescent Dye Molecules*,
  T. Fröhlich, S.-X. Liu, S. Decurtins, C. Schönenberger, and M. Calame.
  Tutorial Course (FUNMOLS) in Bern (Switzerland), February 9-11, 2011.

- *Fluorescence Response in Nanoscale Antennas*,
  T. Fröhlich, C. Schönenberger, and M. Calame.
  SNI-EMPA Workshop on Molecular Electronics in Dübendorf (Switzerland), June 24, 2011.

- *Photoluminescence Response in Nanoscale Antennas*,
  T. Fröhlich, C. Schönenberger, and M. Calame.
  Annual Meeting and School (FUNMOLS) in Barcelona (Spain), September 4-9, 2011.

- *Characterization of Nanoscale Antennas by Gold Photoluminescence*,
  T. Fröhlich, C. Schönenberger, and M. Calame.
  Tutorial Course (FUNMOLS) at IBM Zürich (Rüschlikon, Switzerland), January 15-18, 2012.

- *Gold Photoluminescence in Nanoscale Antennas*,
  T. Fröhlich, C. Schönenberger, and M. Calame.
  Thematic Workshop (FUNMOLS) in Adelsdorf (Germany), May 17-20, 2012.

- *Gold Photoluminescence in Nanoscale Antennas*,
  T. Fröhlich, C. Schönenberger, and M. Calame.
  Annual meeting of the Swiss Physical Society (SPS) at the ETH Zürich (Switzerland), June 21-22, 2012.

- *Gold Photoluminescence in Nanoscale Antennas*,
  T. Fröhlich, C. Schönenberger, and M. Calame.
  Thematic Workshop (FUNMOLS) at Slaley Hall (Newcastle, UK), September 10-13, 2012.

Poster Contributions

- *Towards an Optoelectronic Characterization of Molecules*,
  T. Fröhlich, M. Calame, C. Schönenberger, and O. Martin.
  International Conference on Molecular Electronics (ICME) in Emmetten (Switzerland), January 5-9, 2010.

- *Towards an Optoelectronic Characterization of Molecules*,
  T. Fröhlich, B. Abasahl, M. Calame, C. Schönenberger, and O. Martin.
  Annual Meeting of the Swiss Physical Society (SPS) in Basel (Switzerland), June 21-22, 2010.

- *Electrical and Optical Characterization of Fluorescent Dye Molecules*,
  T. Fröhlich, S.-X. Liu, S. Decurtins, C. Schönenberger, and M. Calame.
  Mid-term Review Meeting and Thematic Workshop (FUNMOLS) in Malvern (UK), September 12-15, 2010.

- *Gold Photoluminescence in Nanoscale Antennas*,
  T. Fröhlich, C. Schönenberger, and M. Calame.
  Thematic Workshop (FUNMOLS) at Slaley Hall (Newcastle, UK), September 10-13, 2012.
- *Gold Photoluminescence in Nanoscale Antennas*,
  T. Fröhlich, C. Schönenberger, and M. Calame.
  Swiss NanoConvention in Basel (Switzerland), May 23-24, 2013.
- *Systematic Investigation of the Gold Photoluminescence in Nanoscale Antennas*,
  T. Fröhlich, C. Schönenberger, and M. Calame.
  MRS Fall Meeting in Boston (USA), December 1-6, 2013.
- *Systematic Investigation of the Gold Photoluminescence in Nanoscale Antennas*,
  T. Fröhlich, C. Schönenberger, and M. Calame.
  APS March Meeting in Denver (USA), March 2-7, 2014.

Curriculum Vitae

Martin **Toni Fröhlich**
born in Berlin (Germany)

Education

- 04/2009 – 09/2014
  University of Basel (Switzerland)
  PhD studies in Experimental Physics (group of Prof. C. Schönenberger):
  "Towards an Optoelectronic Characterization of Molecules by Nanoscale Gold Antennas"

- 11/1998 – 04/2005
  Technical University of Ilmenau (Germany)
  Studies in Technical Physics, Diploma thesis (group of Prof. P. Scharff):
  "Über die Einlagerung von C_{60} in Kohlenstoff-Nanoröhren"

- 08/1994 – 07/1997
  Theodor Fontane Gymnasium in Strausberg (Germany)

Professional Experience

- 04/2009 – 01/2014
  Research assistant, Department of Physics, University of Basel (Switzerland)

- 11/2008 – 03/2009
  Tutor for students, ABACUS Göttingen (Germany)

- 11/2007 – 05/2008
  Research assistant, Laser-Laboratory Göttingen (Germany)

- 02/2006 – 08/2007
  Research assistant, Max Planck Institute of Dynamics and Self-Organization in Göttingen (Germany)
- 05/2002 – 08/2002
  Internship, Weizmann Institute in Rehovot (Israel)
- 2000 – 2003
  Research assistant (occasionally), Institute of Mathematics, Technical University of Ilmenau (Germany)

Grants and Fellowships

- 03/2014
  Marie Curie Alumni Association (MCAA) Micro Travel Grant for participation on the APS March Meeting 2014 in Denver (USA)
- 03/2009 – 02/2012
  Marie Curie Fellowship within the FUNMOLS ITN network (Fundamentals of Molecular Electronic Assemblies)
- 05/2002 – 08/2002
  Karyn Kupcinet International Science School (Israel)
- 11/2001 and 09/2002
  German Academic Exchange Service (DAAD)
  Collaboration with the University of Szeged (Hungary)

Acknowledgements

During my time here in the nanoelectronics group I enjoyed a lot working in a very well-equipped laboratory. Therefore I am happy that Christian Schönenberger gave me the chance to be here. Especially I appreciated that he invested in a new confocal Raman microscope during my PhD period including all the additional upgrades like the motorized stage or the half-wave plates. The main part of my PhD thesis is based on the work with this microscope.

I want to thank Michel Calame for supporting me during the time of my PhD studies, for his scientific advice on break junction measurements and optical issues, and finally for reading the thesis manuscript.

And I also want to mention that the comments of Markus Weiss on the manuscript were very helpful. I thank him as well as Thomas Hasler and Wangyang Fu for reading the document. Especially I am glad that Wangyang Fu and Anton Vladyka were often accompanied me in the office at ungodly hours.

I am very grateful that Jan Brunner and the former colleagues Songmei Wu and Roman Huber introduced me and gave me advice to the break junction measurements. Moreover, I thank Frank Freitag, Cornelia Nef and Peter Rickhaus for their collaboration to maintain the scanning electron microscope and the confocal Raman microscope. I shared several leisure activities together with other members of the huge group. Here are all current and former group members who I have not mentioned yet (in arbitrary order): Andreas Baumgartner, Minkyung Jung, Peter Makk, Romain Maurand, Matthias Bäuninger, Samuel d'Hollosy, Gabor Fabian, Jörg Gramich, Stefan Nau, Vishal Ranjan, Julia Samm, Jens Schindele, Ralph Stoop, Mathias Wipf, Jon Agustsson, Hagen Aurich, Claire Barrett, Alexander Eichler, Oren Knopfmacher, Lukas Hofstetter, Andreas Kleine, Alexey Tarasov, Jelena Trbovic, Haichao Huang, Zheng-Ming Wu, Veronica Savu, Gergö Fülöp and Szabolcs Csonka. Indeed, I was happy to find here people with whom I shared a passion for the mountains. The numerous hikes in the Swiss Alps were all beautiful adventures whether on normal trails, at high altitude, by bicycle or with ski.

Furthermore I was glad to participate in the FUNMOLS network. I thank Martin Bryce (Durham) and all other senior members for organizing thematic workshops

and meetings on molecular electronics. I enjoyed very much the time together with other PhD students of this network: Charalambos Evangeli, Hui Li, Marta Vico Solano, Giorgio Signorello, Pavel Moreno, Andres Ruland, Andrea La Rosa, David Zsolt Manrique, Murat Gulcur and Csaba Peterfalvi.

In Lausanne I want to thank Olivier Martin for the long discussion about my results, Christian Santschi and Banafsheh Abasahl for their scientific advice on gold nanoantennas. Especially I want to mention the simulations of Banafsheh which supports our measurements but are not included in this thesis. In Basel I appreciated a lot that Alexis Baratov could find some time to talk about the optical results, and more precisely about the origin of the interband absorption edge in the spectra.

All technicians and staff members of the mechanical workshop, e.g. Silvester Jakob, Daniel Sacker, Sascha Martin, Stefan Gentsch, Dominik Sifrig and Heinz Breitenstein, were helping me a lot in building several holders for the electron and Raman microscope, mounting gas connections and taking over service work of all kinds. And finally I want to thank Barbara Kammermann and Astrid Kalt for their administrative assistance during my whole time here in Basel.